ATOMIC AND MOLECULAR DYNAMICS IN ULTRASHORT INTENSE LASER FIELDS

by

ZENGXIU ZHAO

B.S., National University of Defense Technology

China, 1993

M.S., National University of Defense Technology

China, 1996

A DISSERTATION

submitted in partial fulfillment of the

requirements for the degree

DOCTOR OF PHILOSOPHY

Department of Physics

College of Arts and Sciences

KANSAS STATE UNIVERSITY

Manhattan, Kansas

2005

Approved By:

Major Professor

Chii-Dong Lin

ABSTRACT

The interaction of ultrashort, intense laser pulses with atomic and molecular systems is studied theoretically. The strong field approximation is applied to describe atomic dynamic processes. We first show the characterization of attosecond pulses from photoionization of Argon atoms assisted by a circularly polarized laser pulse. By studying the angle-resolved photoelectron spectra, we show how to retrieve the electric field of the attosecond pulses by fitting the measured electron spectra using a genetic algorithm.

A quantum theory is further developed to describe the dynamics of an autoionizing state generated by an attosecond XUV pulse in the presence of a femtosecond IR laser pulse. The lifetime of the autoionizing state is determined directly in the time domain from the time-resolved photoelectron spectra. By coherently treating different transition channels, interference effects can be observed. This work extends Fano's theory covering an autoionizing state to the time domain in a time-dependent field.

Compared to atoms, molecules have more degrees of freedom when interacting with laser fields. Because of the different time scales, these motions are generally weakly coupled. We studied the dynamic aligning of molecules by a laser pulse. The experimental observations of ionization suppression of certain molecules suggests the ionization of molecules depends on molecular structure, and thus the alignment of the molecules. We demonstrated the possibility of determining this alignment dependence in a double-pulse configuration. Distinct time dependence of the total ionization yield has been predicted, and the results have been verified by recent experiments.

PUBLICATION LIST

1. "Circularly polarized laser assisted photoionization for attosecond pulse measurements," **Z. X. Zhao**, Zenghu Chang, X. M. Tong and C. D. Lin, Opt. Express **13**, 1966 (2005).
2. "Theory of laser-assisted autoionization by attosecond light pulses," **Z. X. Zhao** and C. D. Lin, to be published on PRA (2004).
3. "Probing molecular dynamics at attosecond resolution with femtosecond laser," X. M. Tong, **Z. X. Zhao** and C. D. Lin, Phys. Rev. Lett. **91**, 233203 (2003).
4. "Correlation dynamics between electrons and ions in the fragmentation of D_2 molecules by short pulses," X. M. Tong, **Z. X. Zhao** and C. D. Lin, Phys. Rev. A **68**, 043412 (2003).
5. "Alignment-dependent ionization probability of molecules in a double-pulse laser field," **Z. X. Zhao**, X. M. Tong and C. D. Lin, Phys. Rev. A **67**, 043404 (2003).
6. "Abnormal pulse duration dependence of ionization probability of Na atoms in intense laser fields," X. M. Tong, **Z. X. Zhao** and C. D. Lin, J. Phys. B **36**, 1121 (2003).
7. "High-order harmonic cutoff extension of the O_2 molecule due to ionization suppression," Bing Shan, Xiao-Min Tong, **Zengxiu Zhao**, Zenghu Chang, and C. D. Lin, Phys. Rev. A **66**, 061401(R) (2002).
8. "Theory of molecular tunneling ionization," X. M. Tong, **Z. X. Zhao**, and C. D. Lin, Phys. Rev. A **66**, 033402 (2002).
9. "Boundary-free scaling calculation of the time-dependent Schrödinger equation for laser-atom interactions," **Z. X. Zhao**, B. D. Esry and C. D. Lin, Phys. Rev. A **65**, 023402 (2002).
10. "Hyperspherical calculations of H(1s)+μ^+ rearrangement collision cross sections," **Z. X. Zhao**, A. Igarashi and C. D. Lin, Phys. Rev. A **62**, 042706 (2000).

11. "Electron interaction with Lithium atoms and Electron impact broadening of the Lithium resonance line," **Zhao Zengxiu**, Yuan Jianmin, Chin. Phys. Lett. **16**,885 (1999).

TABLE OF CONTENTS

PUBLICATION LIST i

LIST OF FIGURES v

ACKNOWLEDGMENTS ix

1. Introduction 1

2. Laser-dressed XUV photoionization: attosecond pulse measurements 8

   2.1 Introduction 8

   2.2 Quantum theory of laser-assisted photoionization 11

   2.3 XUV photoionization of Ar assisted by a circularly polarized laser 14

      2.3.1 Cross section and asymmetry parameter for photoionization of Ar . 16

      2.3.2 Transform-limited XUV pulses 18

      2.3.3 Chirp-dependence 20

      2.3.4 Double XUV pulses 23

   2.4 Retrieving the XUV pulse information 24

   2.5 Conclusions 27

3. Laser-dressed autoionization: time-resolved autoionization spectra 28

   3.1 Introduction 28

   3.2 Quantum theory of laser-assisted Autoionization 29

      3.2.1 Laser-dressed decay of a Lorentzian resonance 29

      3.2.2 Fano resonance theory revisited 32

      3.2.3 Laser-assisted autoionization 34

   3.3 Modeling two-electron systems in laser fields 36

      3.3.1 Construction of the two-channel Hamiltonian 36

      3.3.2 Partial wave expansion 39

      3.3.3 Scattering states with incoming wave boundary conditions 40

3.3.4 Numerical procedure of solving two-channel time-dependent Schrödinger equation . . . 44
3.4 Time-resolved autoionization spectra . . . 45
4. Alignment-dependent ionization of diatomic molecules . . . 52
4.1 Introduction . . . 52
4.2 Alignment of molecules by lasers: The classical rotor model . . . 54
4.3 Adiabatic alignment . . . 55
4.3.1 Classical description . . . 55
4.3.2 Quantum mechanical treatment: Pendular States . . . 56
4.4 Dynamic alignment . . . 57
4.4.1 Kick model and field-free alignment . . . 57
4.4.2 Field-free rotational revival and partial revival . . . 62
4.5 Molecular tunneling ionization theory . . . 65
4.6 Alignment-dependent ionization . . . 69
5. Summary and conclusions . . . 76
Appendix
A. Conversion of units and definiton of parameters . . . 78
B. Gauge transformation . . . 80
C. Program descriptions . . . 82
REFERENCES . . . 89

LIST OF FIGURES

Figure Page

2.1 The time-dependence of the ellipticity and the two perpendicular electric field components of a laser pulse resulting from combining a left-hand circularly polarized pulse and a right-hand circularly polarized pulse. The pulse duration for both circular pulses is 5 fs and the delay between them is 5 fs. The solid and dotted lines represent the two orthogonal field components and the dashed line shows the ellipticity. Note that the small window of vanishing ellipticity or polarization gating where the combined field is nearly linearly polarized . 9

2.2 (a) The square of the dipole transition moment and (b)the asymmetry parameter β from the ground state of Ar by monochromatic light. (c) The ionization probability density vs photoelectron energy of Ar ionized by an XUV pulse which has mean photon energy of 35 eV, duration of 0.1 fs and peak intensity of 10^{12} W/cm^2. Dashed lines represent the spectral shape of the XUV pulse 17

2.3 (a) Energy and angular distributions of photoelectrons from Ar by a single XUV pulse of duration (FWHM) 100 as. The polarization of the XUV pulse is along the x-axis from which the angles of the photoelectrons are measured. (b) and (c), electron spectra by XUV pulses assisted by a circularly polarized laser with phase of $\pi/2$ and 0, respectively. The XUV pulse was assumed to be not chirped 18

2.4 Dependence of photoelectron spectra on the XUV pulse durations. The upper row is for laser-free photoionization and the lower row is for laser-assisted photoionization where the laser phase was chosen to be $\pi/2$. From (a) to (c) the XUV pulse durations are 0.2, 0.5 and 2 fs, respectively. The XUV pulses are assumed to have no chirp 19

2.5 Photoelectron spectra by laser-assisted XUV pulses with different chirp parameters and pulse durations as indicated in the figure. The frequency width of XUV pulse is fixed as 18.25 eV 21

2.6 The center of gravity energy of the photoelectrons vs the electron's angle for different chirp parameters from 0 to 20 of the XUV pulses. The width of the XUV pulse is fixed at 18.25 eV. Note the shift to the higher energy as the chirp parameter increases until at the highest chirp where the pulse duration is close to the optical period 22

2.7 Photoelectron spectra by a train of two attosecond XUV pulses: (a) no laser; (b),(c),(d), with lasers, of phase 0, $\pi/4$ and $\pi/2$, respectively 24

2.8 Comparison of the retrieved electric field with the original field. The inset shows the intensity profile of the original and the retrieved pulses, in units of 10^{12}W/cm^2 25

2.9 Comparison of the photoelectron spectra calculated using (a) the original pulse and (b) the retrieved pulse, at a different time delay of -0.2 fs 26

3.1 Potential curves for a model two-channel system. Black, red and green curves represent V_1, V_2 and V_c respectively. The energy gap between two thresholds is 21.7 eV 46

3.2 Laser-dressed total photoelectron spectrum for an autoionizing state created in XUV+IR laser fields. The spectra from the strong field approximation and from the numerical calculations are shown to agree with each other. The electron spectrum in the absence of lasers is also shown. See text for the parameters used in the calculation 46

3.3 Streaked electron spectra in the forward direction for two Lorentz resonances of lifetime of (a) 0.2 fs and (b) 2 fs, excited by a 0.5 fs XUV pulse. The XUV-laser delay time is zero and two carrier envelope phases are shown: 0 (solid) and π (dashed). For other parameters used, see text. (c) Laser modified electron spectra (black) for a Fano resonance at different time delays. Also shown are the electron spectra of the Lorentz resonance alone (red) and the photoionization alone (green). Parameters for the resonance, the XUV and the laser are as in Fig. 3.2 48

3.4 (a) Electron counts in the forward direction for a Lorentz resonance within the first sideband [20.4,22.1] eV vs time delay, shown for two carrier envelope phases of the laser and the counts after phase average. (b) Similar electron counts for a Fano resonance for electrons within the energy of [20.4,22.1] eV. The smooth curve gives the counts for the corresponding Lorentz resonance part, except vertically shifted by a constant 49

3.5 (a) Streaked electron spectra within the first sideband vs time delay for two nearby Lorentz resonances excited by an attosecond pulse. (b) The oscillatory total electron counts within the sideband vs time delay can be fitted to extract the lifetimes of the two resonances and their energy separation, see text . . 50

4.1 Alignment of N_2 molecules by a laser pulse with intensity 2×10^{13} W/cm^2, duration 250 fs. Dashed line depicts the laser intensity profile. Red line shows the alignment parameter $< \cos^2\theta >$ for N_2 molecule initially in J=0 rotational state. Green lines shows the thermal averaged alignment parameter at room temperature 300 K 60

4.2 Dependence of the maximum alignment on the durations of pump pulses at a peak intensity of 2×10^{13} W/cm^2 for N_2 and O_2 molecules at three temperatures indicated in the plot 63

4.3 Alignment parameter $< \cos^2\theta >$ of N_2 and O_2 molecules at temperature 300K vs time after pumped by a laser pulse with intensity 2×10^{13} W/cm^2 and duration 250 fs 63

4.4 The ionization rates as a function of the angle θ between the laser field direction and the molecular axis for (a) N_2 and (b) O_2 molecules. The laser peak intensity is in units of 10^{13} W/cm^2. The rates are normalized at 0 degree 68

4.5 (a) Ionization signal as a function of the delayed time between the pump and probe laser pulses, and (b) time-dependent alignment parameters after the pump pulse for N_2 at 25 K and 300 K. The pump and probe laser intensities are 2×10^{13}W/cm^2 and 8×10^{13}W/cm^2, respectively 70

4.6 (a) Ionization signal as a function of the delayed time between the pump and probe laser pulses, and (b) time-dependent alignment parameters after the pump pulse for O_2 at 25 K and 300 K. The pump and probe laser intensities are 2×10^{13}W/cm^2 and 8×10^{13}W/cm^2, respectively 71

4.7 (a) Ionization signal as a function of the delayed time between the pump and probe laser pulses with different probe laser polarizations, and (b) time-dependent alignment parameter after the pump pulse for O_2 at 25 K. The pump and probe laser intensities are 2×10^{13}W/cm^2 and 8×10^{13}W/cm^2, respectively 74

ACKNOWLEDGMENTS

I would like to thank my supervising professor Dr. Chii-Dong Lin for constantly motivating and encouraging me and also for his invaluable advice during the course of my doctoral studies. I appreciate his efforts in trying to improve every aspect of my life and my scientific research.

I wish to thank Professor B. D. Esry, Professor Brett DePaola and Professor J. V. Ortiz for taking time to serve on my dissertation committee.

I would also like to thank XiaoMin Tong, XiaoXin Zhou, Toru Morishita, A. Igarashi and B. D. Esry for their collaboration and helpful discussions. I wish to thank Teck Ghee Lee, Shu-Chun Cheng, A. T. Lee, and other present and former members of Professor Lin's group for sharing ideas. I wish to thank the experimentalists: Professor Zenghu Chang, Bin Shan, and Shambhu Ghimire for stimulating and suggestions on my research. My special thanks go to Professor JianMin Yuan for leading me into physics and for providing the opportunities to pursue my dream.

Most of all, I would like to express my deepest gratitude to my wife, Yan Song, for her unconditional love and encouragement and for taking over most of the housekeeping, which made this work possible. I am also extremely grateful to my parents and family at home for supporting me over the years.

Finally I acknowledge the financial support by the Chemical Sciences, Geosciences, and Biosciences Division, Office of Basic Sciences, U. S. Department of Energy.

April 28, 2005

Chapter 1

Introduction

The interaction of an atom with ultrashort intense laser pulses has been studied extensively in the past couple of decades (see review articles [1, 2, 3, 4]). With the rapid development of laser technology, laser pulses have been generated in shorter durations as well as in higher intensities. As the laser intensity approaches 3×10^{16} W/cm^2, the laser-atom interaction is comparable to the atomic potential, and strong field effects, e.g., high order harmonic generation (HHG), tunneling ionization (TI), above threshold ionization (ATI), and stabilization, begin to emerge. On the other hand, as the laser pulse duration is pushed to the femtosecond, or even attosecond region, many atomic dynamic processes can now be resolved or controlled in the time domain with corresponding time resolution. This new frontier poses new challenges not only in theoretical understanding but also in numerical methods for treating atomic processes in ultra-short, intense laser fields.

Single electron ionization of an atom by a short laser pulse is now well understood. The mechanism for ionization can be characterized as a multiphoton transition or tunneling ionization, depending on the Keldysh parameter γ [5], which is defined as $\gamma = \sqrt{\frac{I_p}{2U_p}}$, where I_p is the ionization potential and $U_p = \frac{I}{4\omega^2}$, is the ponderomotive energy of a free electron moving in a laser field with intensity I and frequency ω. The Keldysh parameter measures the ratio of tunneling time to the laser period. If $\gamma < 1$, tunneling ionization is significant, but if $\gamma > 1$, the multiphoton ionization process dominates. The tunneling ionization rate is given by ADK theory [6, 7], which has been shown to agree well with experimental results for single ionization of atoms. However, extending of this theory to multiple ionization of atoms and ionization of molecules has proved to be a challenge, and other physical effects (e.g., sequential and non-sequential double ionization [8, 9] and structure of molecules [10]) need to be taken into account. For multiphoton ionization, electrons can absorb more

photons than the minimum required, leading to the above threshold ionization (ATI) [11]. One interesting problem is to investigate the role of ponderomotive energy in ATI, such as the energy shift of ATI peaks and the vanishing of certain ATI peaks (the so-called channel closing effect) [12, 13, 14].

The interaction of quasi-free electrons with parent ions in the laser pulse leads to high-order harmonic generation (HHG), which can be interpreted as a three-step process. First, the electron tunnels out through the potential barrier formed by the laser field and the atomic potential. Second, the ionized electron moves freely in the laser field, and when the field switches direction, the electron is driven back. Finally, it recombines with the parent ion and emits harmonics. This recollision or rescattering picture [7, 15, 16] is a powerful framework for understanding many laser-atom interaction phenomena. From the classical equation of motion of the electron, the maximum returning energy of the electron is $3.17U_p$ [17]. The HHG spectrum has a generic shape: a rapidly decreasing part, following by a plateau region, and then a rapid decay after the cut-off. The cut-off energy is given by $I_p + 3.17U_p$, which is the maximum recombination energy of the returning classical electron.

The theoretical foundation of the rescattering model lies in the strong field approximation. If the atomic potential is negligible compared to the laser field (close to 1 a.u.) , the electron in the continuum can be treated as a free particle moving in the laser field. Assuming that the laser intensity is in the tunneling region, the contribution of all bound states except the ground state can be neglected. Under these approximations, the time-dependent Schrödinger equation can be solved semi-analytically [18]. This treatment recovers the classical rescattering picture based on the saddle-point analysis. The harmonic generation spectrum can be obtained from the Fourier transformation of the time-dependent dipole moment.

One of the challenges in HHG is to extend the cut-off energy. It has been reported that harmonics of wavelength down to a few nanometers into water window region has been

generated from a 800 nm Ti:Sapphire laser [19]. When the intensity is above saturation intensity, harmonic generation from ions will take over, thus providing a way to extend the cut-off because the ions have higher ionization potential and can be subjected to higher laser intensities [20].

Attosecond Physics:

HHG can be used to generate coherent XUV radiation. In the plateau region, two electron trajectories per half laser cycle have the same recollision energy [21]. Each recollision gives a burst of attosecond radiation; thus the pulse generates an attosecond pulse train [22, 23]. Experimentally observed HHG involves the collective effect of atoms since photon emission is a coherent process. Phase matching is required to propagate light in the medium. Only short trajectories survive after propagation. Since the recollision from the short trajectories repeat every half of the laser cycle, the resulted spectrum is discrete, and separated by 2ω. However, in the cut-off region, the HHG from a few-cycle laser pulse is much smoother, because the highest harmonics are generated by a single-electron trajectory close to the peak without possible periodicity, which suggests an isolated attosecond burst of radiation [24, 3].

Based on the rescattering picture for HHG, isolated attosecond pulses can be generated in two ways. One is to take advantage of the harmonics generated in the cut-off region. By selecting the radiation produced only within a fraction of the laser cycle near the peak of the pulse using a filter, XUV pulses of about 100 attoseconds (as) duration can be generated [25, 24, 26]. Another approach is to control the trajectories of the rescattering electron by using polarization gating [27, 28, 29]. Elliptically polarized light gives a transverse momentum to ionized electrons, thus making them miss the parent ions upon return and resulting in very weak HHG. Only electrons born within the linear part of the pulse contribute to HHG. When the time interval in the linear part is short enough, one single burst of attosecond radiation is emitted. The efficiency of this method is low because only

a small fraction of the pulse is used for harmonic generation. On the other hand, it does overcome the limitation of the low intensity of HHG in the cut-off region.

The carrier-envelope (CE) phase (absolute phase) of few-cycle laser pulses is crucial for laser stimulated physical processes like HHG [30, 31] and rescattering ionization [32, 33, 34]. Though phase stabilization has been achieved [35, 36, 37], the measurement of the CE phase is more difficult. Various approaches have been proposed, based on, for example, the sensitivity of angular distribution of photoelectrons [32, 14, 34], phase-dependent HHG [30, 37], and tunneling ionization by a circularly polarized pulse [38].

The current status of attosecond physics has been reviewed in [39, 3, 4]. As the shortest pulses available in the laboratory, attosecond XUV pulses can be used to resolve many atomic dynamic processes involving electronic motion in the time domain. As a first proof-of-principle application of attosecond pulses, the Auger lifetime of an inner shell hole was determined in the time domain by Drescher *et al.* [40]. By stabilizing the CE phase, electronic processes in intense light fields are controlled at the sub-femtosecond scale [37]. In order to prove the existence of attosecond pulses, characterization and measurements are developed at the same time. Because of the (so far) weak intensity of XUV pulses generated and a lack of nonlinear media working in this wavelength region, measurement techniques rely on the cross-correlation of the XUV pulse with an IR femtosecond pulse in two-color photoionizations [41, 42, 43, 44]. Single attosecond pulses with a duration of 700 as have been measured [45, 46, 47] recently in a laser-assisted photoionization experiment. The same technique can directly measure the light field[48]. Pulse trains are measured from two-photon, two-color photoionization [22, 49] as well.

All the measurements still have to be carried in the energy domain, so it is theoretically a challenge to extract dynamic information from the time-resolved spectra. Full *ab initio* calculation of a dynamically evolving system in light fields is difficult and time-consuming because of the large parameter space. However, by grasping the essential physics,

semi-analytical quantum mechanical models have been developed for laser-assisted photoionization [43], time-resolved Auger decay [40, 50, 51], and laser-assisted autoionization [52]. The excitation or ionization by the XUV pulse can be treated perturbatively because of its weak intensity. The evolution of the system in a laser pulse thus can be treated semi-classically under the strong field approximation. By varying the time-delay between the two pulses, the time-resolved laser-dressed electron spectrum provides insight into the dynamics of the system.

Laser-Molecule Interactions:

Recently, basic mechanisms involving laser-molecule interactions have been probed at more fundamental levels, owing to the wide availability of intense femtosecond laser pulses, with pulse durations in the tens of femtoseconds and the use of OPAs to cover a broader range of mean wavelengths. With such controls, the interplay of electronic dynamics, the rotational motion, and the vibrational motion, including dissociation and ionization, can be probed with a broad range of parameters (see review articles [53, 54]).

The tunneling ionization rates of molecules are very similar to atoms if they have nearly identical ionization potentials. However, a detailed study found exceptions [55, 56, 57, 58, 59]. The origin of ionization suppression of some molecules was explained in [10]. The ADK theory of tunneling ionization for atoms has been extended to diatomic molecules by including the properties of molecular orbitals into the theory; thus, the so-called MO-ADK theory was developed [10]. This theory not only interpreted the origin of ionization suppression for certain molecules but also predicted that the cutoff of the high-order harmonics would be extended for molecules like O_2 but not for N_2. Such predictions have been confirmed in experimental research [60]. The ionization probability of molecules, according to the MO-ADK theory, showed dependence on the alignment of the molecules. In order to check such dependence, aligned molecules are required (see review article [54]). Molecules can be aligned during periods of rotational revival after being pumped by a

prepulse so the alignment-dependent ionization can be determined in a double-pulse measurement [61, 62, 63]. Alternatively, the alignment dependence can also be probed from the angular distributions of the ion fragments following double ionization. To ensure that the laser field does not contribute to the alignment before the ionization and that post-ionization alignment [64] is negligible, sub-10 fs weaker laser pulses (less than 10 fs) have been used to doubly ionize the molecules in the so-called nonsequential double ionization region where the second ionization is by nearly isotropic rescattering. This method has been used by Professor C. L. Cocke's group at Kansas State University to probe alignment dependence for a number of molecules [65].

By detecting fragments from dissociation and analyzing the kinetic energy release, some basic processes of molecules in intense laser fields have been identified, like bond softening [66], bond hardening [67], above-threshold dissociation and charge resonant enhanced ionization (CREI) [68]. The avoided crossings of the photon-dressed states in the Floquet picture is the key to interpreting most of these processes. However, the dynamics are not time-resolved directly, and the Floquet picture is questionable when the pulse is only a few cycles long.

The generation of attosecond pulses from high-order harmonics generation implies sub-laser-cycle electronic dynamics. The rescattering of the tunneling electrons can lead to double ionization (Coulomb explosion), to excitation and dissociation of molecules that provides a natural way to probe the molecular dynamics in a sub-femtosecond scale [69]. The ionization of the first electron launches a pair of correlated nuclear and electronic wave packets and starts the molecular clock. The second ionization of the molecular ion from rescattering sets the "stop" time. By measuring the kinetic energy release following Coulomb explosion, the time between the ionization events can be determined to attosecond accuracy [70, 71]. Because of the high current densities (8×10^{10} A/cm^2 and short time

scale (about 1 fs), the rescattering electrons may potentially serve as a natural pulsed beam to image molecular structures [72] as well.

Outline of this thesis

The next two chapters will focus on attosecond physics. In Chapter 2, we examine the possibility of retrieving the electric field of an XUV attosecond pulse generated by polarization gating. A genetic algorithm is applied to fit the angle-resolved photoelectron spectra of Argon by XUV pulses assisted by a femtosecond circularly polarized laser. In Chapter 3, we present the theory of laser-assisted autoionization by an XUV attosecond pulse and discuss the determination of Fano parameters from the time-resolved electron spectrum. Alignment of molecules by a laser pulse is discussed in Chapter 4. The alignment-dependent ionization of diatomic molecules N_2 and O_2 is discussed in the context of a double pulse experiment. A summary and conclusion is given in Chapter 5.

Chapter 2

Laser-dressed XUV photoionization: attosecond pulse measurements

2.1 Introduction

Single attosecond extreme ultraviolet (XUV) or soft x-ray pulses can be generated by high-order harmonic generation with few-cycle femtosecond infrared (IR) laser pulses [3]. Their short wavelength and weak intensity means that the conventional autocorrelation method cannot be used to determine their pulse durations directly. So far, pulse duration has been determined with laser-assisted photoionization where photoelectron spectra by XUV pulses are measured in the field of the IR lasers. By varying the time delay between the laser and XUV pulses, their cross-correlation is built either by the laser-induced energy shift [46] or by the laser-broadened spectral width [45]. Based on the quantum mechanical formulation of laser-dressed photoionization [43, 44], pulse duration of a few hundred of attoseconds [46] has been determined from experimentally measured photoelectron spectra. Most recently, this technique has also been used to characterize directly the electric field of a few-cycle laser pulse [48]. In the generating and characterizing of XUV pulses from these time-resolved measurements, so far only linearly polarized lasers have been used.

An alternative approach to making single attosecond pulses is through high-order harmonic generation using the polarization gating method [73, 27, 74, 28, 75, 29]. Using a laser composed of two opposite circular polarizations, a supercontinuum covering the plateau and the cutoff region of the harmonic spectrum has been recently generated [76]. This method is illustrated in Fig. 2.1. By superimposing a left-circularly polarized pulse of about 5 fs with a delayed (by about 5 fs) right-circularly polarized pulse, the ellipticity of the combined pulse is almost zero over a short time interval near t=0 [29]. In Fig. 2.1, it can be seen that within this interval, less than an optical cycle, the electric field of one of the two orthogonal components vanishes, and the electric field is almost linearly polarized. The

radiation generated from such a pulse can be calculated, and a supercontinuum spectrum is generated. This supercontinuum showed correspond to XUV pulses as short as 200 as. However, this duration has not been determined experimentally as yet. For my thesis, we developed a technique that can be used to measure the time-dependent electric field of the attosecond pulses. The method employs the cross correlation between the attosecond pulses with the circularly polarized lasers that were used to generate the attosecond pulse.

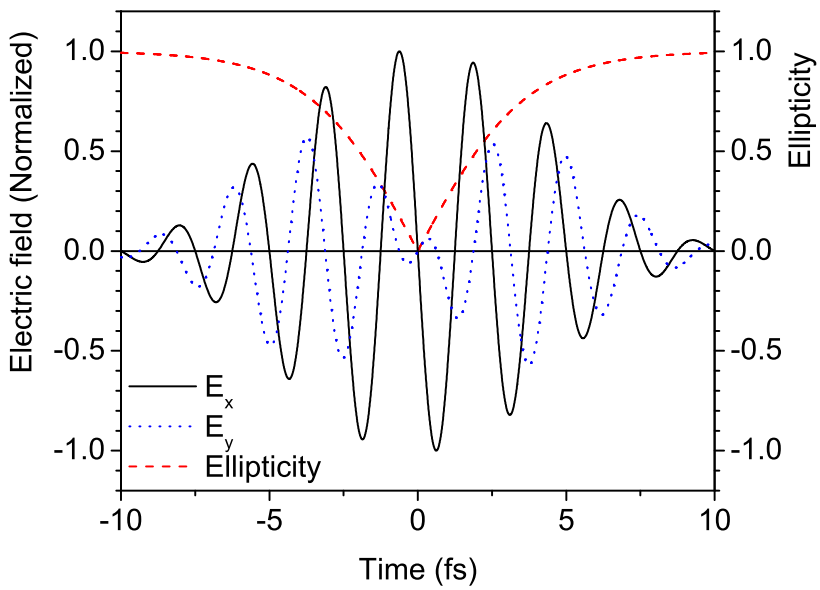

Figure 2.1. The time-dependence of the ellipticity and the two perpendicular electric field components of a laser pulse resulting from combining a left-hand circularly polarized pulse and a right-hand circularly polarized pulse. The pulse duration for both circular pulses is 5 fs and the delay between them is 5 fs. The solid and dotted lines represent the two orthogonal field components and the dashed line shows the ellipticity. Note that the small window of vanishing ellipticity or polarization gating where the combined field is nearly linearly polarized.

In such measurements, the attosecond pulse will be delayed by approximately 5 fs so that the generated photoelectrons only interact with the portion (t>5 fs) of the laser pulse

that is almost circularly polarized. To simplify the analysis, we used an ideal circularly polarized field to represent the laser. By refocusing the XUV pulse and the fundamental circularly polarized laser into the argon gas, the XUV pulse characterization was determined from the measured angle-resolved photoelectron spectra. Such a setup involved XUV photoionization assisted by a short circularly polarized laser. The basic theory for such cross correlation measurement has been addressed by Itatani *et al.* [44]. In this work, we examined in detail the laser streaked photoelectron spectra by taking the angle-dependent photoionization cross section into account. We first studied theoretically the angle-resolved photoelectron spectra for such experiments by changing the attosecond pulse parameters, in particular, the pulse durations and the chirp parameters. We illustrated how the electron spectra changed with these parameters. From the calculated electron spectra, we then showed how to retrieve the attosecond XUV pulse parameters. This technique is expected to be used to determine the attosecond pulses in the time domain when electron spectra from such cross correlation experiments become available.

The quantum theory of laser-assisted photoionization is reviewed in Section 2.2. In Section 2.3, we address the photoionization of Ar atoms by monochromatic light. The atomic structure parameters from these calculations will be used in Section 2.4 to generate "theoretical" photoionization electron spectra by attosecond pulses in the presence of circularly polarized lasers. Thereafter, we explore how the electron spectra changed with the pulse duration, and then how they changed with the chirp. In Section 2.5, we discuss how to retrieve the attosecond XUV pulse parameters from the given angle-resolved electron spectra. Finally, we give a short conclusion on this chapter in Section 2.6. Atomic units will be used throughout unless otherwise indicated.

2.2 Quantum theory of laser-assisted photoionization

Consider an atom in a single-electron approximation under the influence of a laser field. The time-dependent Schrödinger equation (TDSE) in the length gauge is given by

$$i\frac{\partial\Psi(\vec{r},t)}{\partial t} = \left[-\frac{1}{2}\nabla^2 + V(\vec{r}) - \vec{r}\cdot\vec{E}(t)\right]\Psi(\vec{r},t), \tag{2.1}$$

where $V(\vec{r})$ is the atomic potential and $E(t)$ is the external laser field. Dipole approximation is applied for the laser-atom interaction. To solve this equation, we make the following assumptions (strong field approximation):

1. No depletion of the ground state;
2. Neglect the influence of Coulomb field on the electrons in the continuum so that they can be treated as free particles moving in the laser field (Volkov state);
3. No other intermediate bound states contribute, i.e., assume that the atom has only one bound state and continua.

The time-dependent wave function can be expanded as

$$\Psi(\vec{r},t) = e^{iI_p t}\left(|0> + \int d\vec{p}\, b(\vec{p},t)|\vec{p}>\right), \tag{2.2}$$

where I_p is the ionization potential of the ground state $|0>$, and $|\vec{p}>$ denotes the continuum electron with momentum $\vec{p}$. The TDSE can be solved semi-analytically in this approximation, and the amplitude of the continuum electron $|\vec{p}>$ is given by

$$b(\vec{p},t) = i\int_{-\infty}^{t} dt_1 \sum_{\vec{p'}} <\vec{p}|\vec{p'}(t,t_1)><\vec{p'}(t,t_1)|\vec{r}\cdot\vec{E}(t_1)|0> e^{iI_p(t_1-t)} \tag{2.3}$$

where $|\vec{p'}(t,t_1)>$ is the Volkov state describing a free particle moving in a laser field and is given by

$$|\vec{p'}(t,t_1)>= \frac{1}{(2\pi)^{3/2}} e^{i(\vec{p}+\vec{A}(t)-\vec{A}(t_1))\cdot\vec{r}} e^{i\int_{t_1}^{t} dt''(\vec{p}+\vec{A}(t)-\vec{A}(t''))^2/2}, \tag{2.4}$$

where $\vec{A}(t)$ is the vector potential related to the electric field by

$$\vec{E}(t) = -\frac{\partial\vec{A}}{\partial t}. \tag{2.5}$$

The transition amplitude can be written explicitly as given in [18]:

$$b(\vec{p},t) = i\int_{-\infty}^{t} dt_1\, \vec{E}(t_1)\cdot\vec{d}[\vec{p}+\vec{A}(t)-\vec{A}(t_1)]\exp\{-i\int_{t_1}^{t} dt''[\frac{(\vec{p}+\vec{A}(t)-\vec{A}(t''))^2}{2}+I_p]\}, \quad (2.6)$$

where $\vec{d}(\vec{p})$ is the dipole transition moment from the ground state to the continuum $|\vec{p}>$. This equation has been derived in length gauge [5, 18], in acceleration gauge [77], and in velocity (radiation) gauge [78]. The transformation between different gauges is given in Appendix B.

The strong field approximation has been proved to be powerful and is extensively used in studying HHG and ionization. Once the transition amplitudes to the continua are obtained, the induced dipole moment, and thus high-order harmonic generation, can be calculated directly [18]. The S-matrix form of this formulation is also used for calculating above-threshold ionization and multiple ionizations [79, 80, 81].

This approximation is further applied to the two-color photoionization of atoms by a combination of a linearly polarized XUV pulse and a linearly or circularly polarized laser pulse [43, 44]. In such a setup, the cross correlation of the two pulses is established through the laser-assisted photoionization, which provides a possible way of measuring the duration (a few hundred attoseconds) of the short XUV pulse. The photoelectron spectrum, if we rewrite the formula above, is given by

$$\begin{aligned} b(\vec{p},t) &= i\int_{-\infty}^{t} dt'\, \vec{E}(t')\cdot\vec{d}[\vec{p}+\vec{A}(t)-\vec{A}(t')] \\ &\times\exp\{-i\int_{t'}^{t}\frac{[\vec{p}+\vec{A}(t)-\vec{A}(t'')]^2}{2}dt''+iI_P t'\}. \end{aligned} \quad (2.7)$$

When t goes to ∞, the vector potential vanishes (as our choice), and we have

$$\begin{aligned} b(\vec{p}) &= i\int_{-\infty}^{\infty} dt'\, \vec{E}(t')\cdot\vec{d}[\vec{p}-\vec{A}(t')] \\ &\times\exp\{-i\int_{t'}^{\infty}\frac{[\vec{p}-\vec{A}(t'')]^2}{2}dt''+iI_P t'\}. \end{aligned} \quad (2.8)$$

By considering the different photon energy scales of the XUV and the laser field, this can be further simplified. For a weak laser field, ionizations by the laser field itself can only go through a multiphoton process. In the non-resonant case, multiphoton ionizations are much weaker than ionizations by single photon. Thus in the process of generating the continuum, we can neglect the contribution of the laser field. This assumption can be checked numerically by calculating the ionization probability by the laser field and by the XUV pulse individually. In propagating of the free electron in the field, we neglect the XUV pulse, since the vector potential is inversely proportional to the photon energy.

The integral over time can be performed by the stationary phase method, i.e., only the times that electrons born at the saddle point t_s contribute mostly to integration. The saddle points satisfy the stationary phase equation

$$\frac{1}{2}[\vec{p} - \vec{A}(t_s)]^2 = W_0 \tag{2.9}$$

that expresses the conservation of energy in laser-dressed photoionization, where W_0 is the electron energy given by $\hbar\omega_x - I_p$ at birth. For a laser field linearly polarized along the XUV polarization direction, recasting this equation, the kinetic energy of the photoelectron is obtained as

$$W_p = W_0 + U_p(t)(\cos 2\omega_l t_s - 1) + 4U_p(t_s)\sin^2\omega_l t_s \cos^2\theta + \sqrt{8W_0 U_p(t_s)}\sin\omega_l t_s \cos\theta, \tag{2.10}$$

where θ is the angle of the electron final momentum with respect to the XUV (and laser) polarization direction.

We can reformulate the equation above as shown in [44]. Defining the angle between final momentum $\vec{p}$ and birth momentum $\vec{p_0}$ ($\frac{p_0^2}{2} = \hbar\omega_x - I_p$) as β, we have

$$p = A\cos\theta + p_0\cos\beta, \tag{2.11}$$

$$A\sin\theta = p_0\sin\beta, \tag{2.12}$$

and

$$W_p = A^2 \cos^2 \theta/2 + W_0 \cos^2 \beta + AP_0 \cos\theta \cos\beta. \tag{2.13}$$

Recognizing

$$\cos\beta = \pm\sqrt{1 - A^2 \sin^2 \theta/p_0^2}, \tag{2.14}$$

we have

$$W_p = W_0 + 2U_p(t) \sin^2 \omega_l t \cos 2\theta + \cos\beta\sqrt{8W_0 U_p(t)} \sin\omega_l t \cos\theta. \tag{2.15}$$

For a circularly polarized laser field given by

$$\frac{1}{\sqrt{2}} E[\cos(\omega_l t)\vec{e}_x + \sin(\omega_l t)\vec{e}_y], \tag{2.16}$$

the expression of the photoelectron kinetic energy can be generalized as

$$W_p = W_0 + U_p(t) \cos 2(\omega_l t - \theta) + \cos\beta\sqrt{4W_0 U_p(t)} \sin(\omega_l t - \theta) \tag{2.17}$$

with

$$\cos\beta = \pm\sqrt{1 - \frac{A^2}{2} \sin^2(\omega_l t - \theta)/p_0^2}. \tag{2.18}$$

2.3 XUV photoionization of Ar assisted by a circularly polarized laser

Let us consider photoionization of Ar atoms by XUV pulses assisted by a circularly polarized laser field. Electrons that are born at different times within the XUV pulse gain additional time-dependent drift velocity from the laser field, which is rotating in time. The XUV pulse with duration τ_x and photon energy ω_x can be generally described by

$$\vec{E}_x(t) = Re\{E_{0x} e^{-\sigma(1-i\xi)t^2} e^{i\omega_x t} \vec{e}_x\}, \tag{2.19}$$

where $\sigma = 2\ln 2/\tau_x^2$, and ξ is a dimensionless chirp parameter. The XUV pulse is linearly polarized along x direction with intensity 10^{12} W/cm^2 and mean photon energy 35 eV. A circularly polarized laser field is characterized by an electric field

$$\vec{E}_l(t) = \frac{1}{\sqrt{2}} E_0(t)[\cos(\omega_l t + \phi)\vec{e}_x + \sin(\omega_l t + \phi)\vec{e}_y], \tag{2.20}$$

that has a Gaussian shape with FWHM of 5 fs, intensity of 5×10^{13}W/cm^2. The central wavelength of the laser is taken to be 750 nm.

For electrons born at time t, a drift momentum (proportional to the vector potential of the laser field) given by

$$\vec{A}_l(t) = \int_t^\infty \vec{E}_l(t)dt \tag{2.21}$$

will be added to the photoelectron. For the convenience of analysis, if the envelope is slow varying, the drift momentum can be approximated by

$$\vec{A}_l(t) \cong \frac{1}{\sqrt{2}\omega_l} E_0(t)[-\sin(\omega_l t + \phi)\vec{e}_x + \cos(\omega_l t + \phi)\vec{e}_y]. \tag{2.22}$$

According to the strong-field approximation [5, 18] as discussed in the previous section, the laser-assisted photoelectron spectrum is given by [43, 44]

$$b(\vec{p}) = i\int_{-\infty}^{\infty} dt \vec{d}(\vec{p'}(t)) \cdot \vec{E}_x(t) \exp\left[-i\int_t^\infty dt' \frac{p'(t')^2}{2} + iI_p t\right], \tag{2.23}$$

where $b(\vec{p})$ is the amplitude of finding the continuum electron with momentum $\vec{p}$, $\vec{p'}(t) = \vec{p} - \vec{A}_l(t)$ is the instantaneous momentum of electron at time t, and I_p is the ionization energy. From the saddle point analysis, most of the contribution to the time integral comes from the time t_s satisfying the stationary phase condition given by Eq. 2.9; and the classical model is thus developed in [46, 45]. However, in the calculation, integration over time in Eq. 2.23 is performed numerically.

2.3.1 Cross section and asymmetry parameter for photoionization of Ar

For simplicity, we first consider single ionization of Ar atoms by a monochromatic XUV light. We used the single active electron model where the argon atom is described by a model potential [82]

$$V(r) = -(1 + 5.4e^{-r} + 11.6e^{-3.682r})/r. \tag{2.24}$$

Starting from the occupied 3p orbital, the electron is released to s-wave or d-wave continuum through one-photon photoabsorption. The radial dipole matrix elements to ϵs (R_-) and ϵd (R_+) continuum states are given by

$$R_{-(+)} = \int_0^\infty r P_{3p} P_{\epsilon s(\epsilon d)} dr, \tag{2.25}$$

where the P's are the r-weighted radial wavefunctions. Because there are six 3p valence electrons in the ground state of argon, the total cross section σ_{tot} is proportional to

$$|d|^2 = 6(\frac{1}{3}R_-^2 + \frac{2}{3}R_+^2), \tag{2.26}$$

where d is the magnitude of the total transition dipole moment.

The angular distribution of the photoelectrons by a linearly polarized light is given by

$$\frac{d\sigma}{d\Omega} = \frac{\sigma_{tot}}{4\pi}\left[1 + \beta\frac{3\cos^2\theta - 1}{2}\right], \tag{2.27}$$

where θ is the angle of the electron's final momentum with respect to the light polarization direction, and β is the asymmetry parameter that can be calculated using the method described in [83]. Knowing the β parameter and the total transition dipole moment, in the same spirit of obtaining the differential cross section, we can define an effective angular dependent transition dipole moment for later calculating laser-assisted photoionization.

Figure. 2.2 shows the calculated (a) $|d|^2$ and (b) the β parameter versus the photon energy of the monochromatic XUV light. The results from this simple calculation show

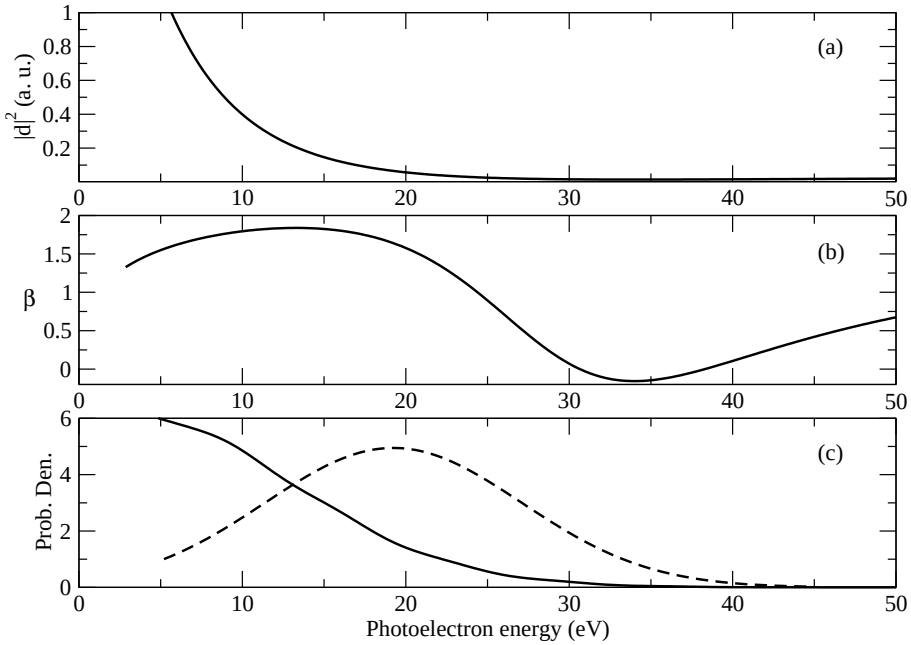

Figure 2.2. (a) The square of the dipole transition moment and (b)the asymmetry parameter β from the ground state of Ar by monochromatic light. (c) The ionization probability density vs photoelectron energy of Ar ionized by an XUV pulse which has mean photon energy of 35 eV, duration of 0.1 fs and peak intensity of 10^{12} W/cm^2. Dashed lines represent the spectral shape of the XUV pulse.

reasonably good agreement with the more elaborate many-electron calculations [84, 85], including the position of the Cooper minimum. A direct numerical solution of the time-dependent Schrödinger equation for the ionization of argon atom in a short XUV pulse has also been carried out under the single-active electron approximation with these pulse parameters: mean photon energy, 35 eV; pulse duration, 100 attoseconds (as); peak intensity, 10^{12} W/cm^2. The photoelectron spectrum from such a calculation is presented in Fig. 2.2(c). The interaction is in the perturbation regime, so the spectral intensity distribution of the XUV pulse can be obtained by dividing the electron spectral density by the photoionization cross section, as shown in the dashed lines in Fig. 2.2(c). Assuming that the pulse

is transform-limited, the XUV pulse in the time-domain is obtained directly by a simple Fourier transformation. However, such an assumption is not generally valid.

2.3.2 Transform-limited XUV pulses

First we consider transform-limited XUV pulses for which the chirp parameter is zero. XUV pulse parameters are chosen as in Fig. 2.2. Note that an XUV photon energy of 35 eV corresponds to the 21st-order high harmonics from the Ti:Sapphire laser field with a wavelength 750 nm. Laser intensity was chosen to be 5×10^{13} W/cm^2 so that the ionization probability by the XUV itself (intensity is 10^{12} W/cm^2) is two orders higher than the ionization probability by the laser field (from the ADK theory). The two pulses peak at the same time, $t = 0$. The polarization direction of the XUV pulse is defined as the x-axis (zero angle). The drift velocity at $t = 0$ is along y direction if the laser phase is zero and -x direction if laser phase is $\pi/2$.

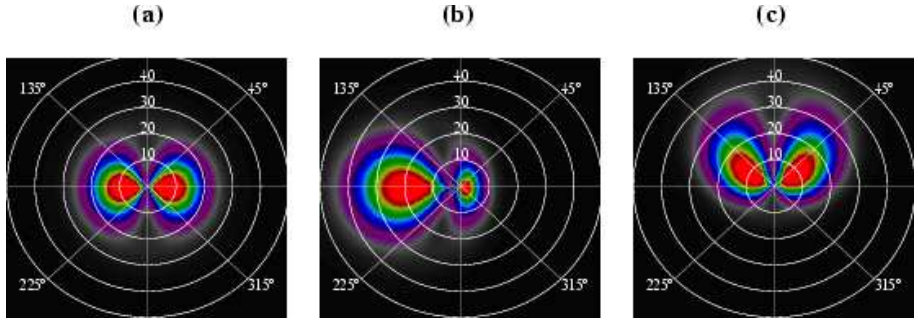

Figure 2.3. (a) Energy and angular distributions of photoelectrons from Ar by a single XUV pulse of duration (FWHM) 100 as. The polarization of the XUV pulse is along the x-axis from which the angles of the photoelectrons are measured. (b) and (c), electron spectra by XUV pulses assisted by a circularly polarized laser with phase of $\pi/2$ and 0, respectively. The XUV pulse was assumed to be not chirped.

For XUV photon energy of 35 eV, the asymmetry parameter β is approximately 1.5, thus the laser-free photoelectrons peak at 0 and 180 degrees as shown in Fig. 2.3(a).

(Because of the stronger signal along the XUV polarization direction (x-axis), a smaller detection angle is required when the detector is along the x-axis.) When a laser field is present, the spectrum is deformed. Fig. 2.3(b) and Fig. 2.3(c) show the laser-assisted photoelectron spectra for laser phase of $\pi/2$ and 0, respectively. The spectra are calculated from Eq. 2.23. When the drift velocity is along the $-x$ direction ($\phi = \pi/2$; Fig. 2.3(b)), more electrons are found in the $-x$ direction, and the energy distribution is stretched in the same direction, makeing the detection more efficient than for the laser phase 0 (Fig. 2.3(c)). Clearly, a phase-stabilized laser with the phase of $\phi = \pi/2$ is more desirable. In the following, we will only consider the laser phase $\phi = \pi/2$ unless otherwise indicated.

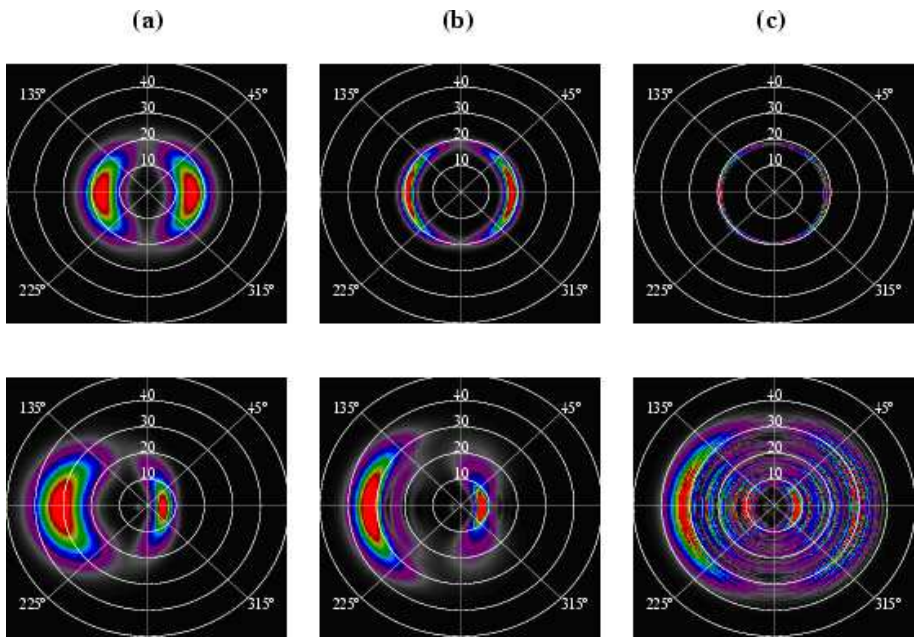

Figure 2.4. Dependence of photoelectron spectra on the XUV pulse durations. The upper row is for laser-free photoionization and the lower row is for laser-assisted photoionization where the laser phase was chosen to be $\pi/2$. From (a) to (c) the XUV pulse durations are 0.2, 0.5 and 2 fs, respectively. The XUV pulses are assumed to have no chirp .

Figure 2.4 shows how the electron spectra change with increasing XUV pulse duration. As XUV duration increases, the energy width of laser-free photoelectron spectra decreases. On the other hand, when a circularly polarized laser is present, the distribution of the drift velocity that the electrons gain during the XUV pulse duration becomes broader in the angle; thus the resulting photoelectron spectra show increasing angular width. When the XUV pulse duration approaches the laser period (Fig. 2.4(c)), ring-like sideband structures appear following the trajectory of laser's vector potential. The ring-like structures were also observed for linearly polarized laser-assisted photoionization by a train of attosecond pulses [49].

In short, if the XUV pulses are transform-limited, we have:

1. The electron energy width for a given angle decreases as the XUV pulse duration increases.
2. The electron angular width for a given energy becomes broader as XUV pulse duration increases.
3. The electron's momentum image extends in all directions, and sideband structure begins to emerge as the XUV pulse duration approaches the laser's optical period.

Based on the pulse duration dependence of the spectra, the duration of the attosecond pulse might be deduced by mapping the measured electron velocity image in accordance with the principle of frequency resolved optical gating (FROG) [86]. As suggested by Itatani *et al.* [44], the pulse duration can be retrieved from the angular distribution of electron momentum at a given energy. We will discuss this further.

2.3.3 Chirp-dependence

In the previous section, we discussed how the electron spectra change with the duration of the XUV pulses when they are transform-limited. However, for transform-limited XUV pulses, the pulse duration can be obtained directly from the bandwidth of the photo-

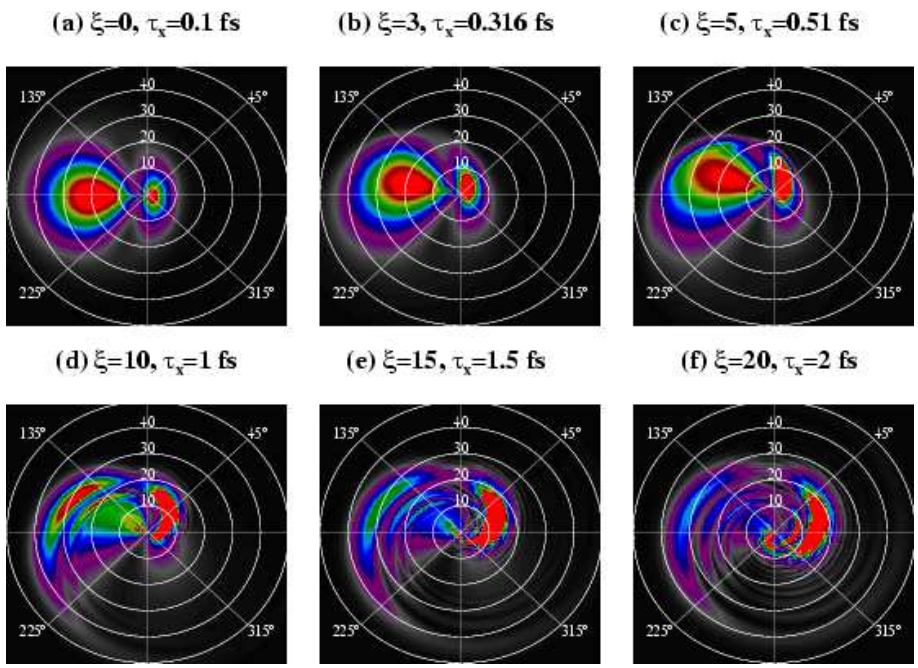

Figure 2.5. Photoelectron spectra by laser-assisted XUV pulses with different chirp parameters and pulse durations as indicated in the figure. The frequency width of XUV pulse is fixed as 18.25 eV.

electron energy spectrum at any angle, without applying the laser field, as discussed earlier. In general, the chirp parameter of the XUV pulse has to be determined in order to obtain the pulse duration.

For the XUV pulse described in Eq. 2.19, with nonzero chirp parameter, the frequency bandwidth is given by

$$\Delta\omega = \frac{4\ln 2}{\tau_x}\sqrt{1+\xi^2}. \tag{2.28}$$

We will examine laser-assisted electron spectra with fixed frequency bandwidth by varying the pulse duration and the chirp ξ simultaneously. In Fig. 2.5, we present six cases of chirp parameters and pulse durations: (a) ξ=0, τ_x=0.1 fs; (b) ξ=3, τ_x=0.32 fs; (c) ξ=5, τ_x=0.51 fs; (d) ξ=10, τ_x=1 fs; (e) ξ=15, τ_x=1.51 fs; and (d) ξ=20, τ_x=2 fs.

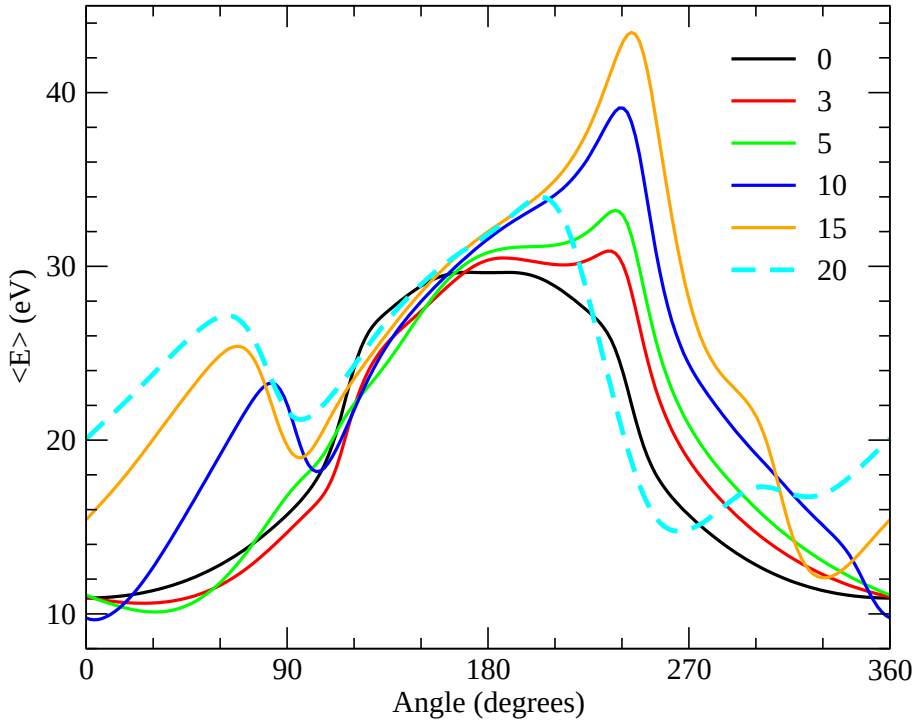

Figure 2.6. The center of gravity energy of the photoelectrons vs the electron's angle for different chirp parameters from 0 to 20 of the XUV pulses. The width of the XUV pulse is fixed at 18.25 eV. Note the shift to the higher energy as the chirp parameter increases until at the highest chirp where the pulse duration is close to the optical period .

With the XUV pulse frequency bandwidths fixed, the laser-free photoionization spectra are the same for all the six cases (if neglecting the final energy dependence of the dipole transition moment). Thus, the pulse duration can not be resolved by XUV photoionization alone. As the chirp increases from (b) to (f), the spectral image twists and splashes toward the left (we used left-circularly polarized laser). This behavior can be understood from the modified stationary phase equation:

$$\frac{1}{2}[\vec{p} - \vec{A}_l(t)]^2 = E_0 - 2\sigma\xi t = \Omega(t). \tag{2.29}$$

In contrast to the zero-chirp case, in a chirped pulse, the electron is born with a time-dependent instantaneous energy. Thus, the final electron momentum is not just rotated by

the laser field but also stretched in magnitude because of the chirp. In this case, we cannot determine the pulse duration from the angular distribution of the electron momentum at a given energy. Instead, at each angle, we can define the center of gravity energy $E(\theta)$ (see Fig. 2.6). By focusing on this trace for angles larger than 180°, we note that $E(\theta)$ increases monotonically with increasing chirp, until we reach the large chirp parameter of 20 where the duration of the XUV pulse of 2.0 fs is close to the laser period. This trace, combining with the angular width, qualitatively illustrates the chirp and pulse duration dependence of the XUV pulses in the time-domain.

2.3.4 Double XUV pulses

Next we consider a pulse train consisting of double pulses without chirp, separated by $T_0/2$ (i.e., half the laser period),

$$E_x(t - T_0/4) + E_x(t + T_0/4), \tag{2.30}$$

Each pulse has a duration of 0.2 fs and a corresponding peak intensity 10^{12} W/cm^2. When the polarization gating is not short enough, such a train of two attosecond pulses is generated. In this case, the duration of each pulse (within the pulse train) can still be retrieved.

For such a pulse train, the laser-free photoelectron energy spectra consist of two rings separated by $2\omega_l$; see Fig. 2.7(a). When the laser field is present, the spectra are distorted but have two identical pairs. In Fig. 2.7, the laser phases are 0, $\pi/4$, $\pi/2$; from (b) to (d), respectively. In (b) electrons generated by the left pulse show a $+x$ shift, while electrons generated by the right pulse show a $-x$ shift. Thus, the total electron spectra are stretched along the x-axis. In (c), electrons generated by the two pulses shift about half way toward the 45 degree (and 225 degree) line. In (d), the shift to this diagonal line is complete, and the electron spectra have a butterfly shape.

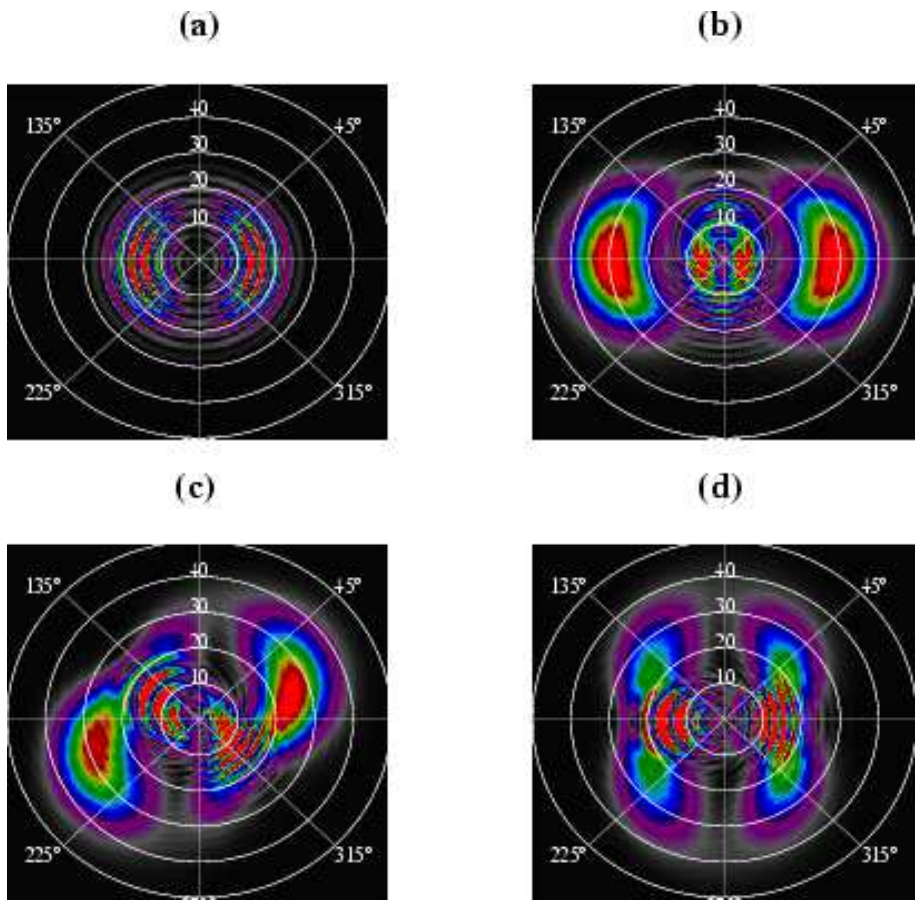

Figure 2.7. Photoelectron spectra by a train of two attosecond XUV pulses: (a) no laser; (b),(c),(d), with lasers, of phase 0, $\pi/4$ and $\pi/2$, respectively.

2.4 Retrieving the XUV pulse information

The laser-free photoionization spectrum is obtained from this equation:

$$b(\vec{p}) = i \int_{-\infty}^{\infty} dt\, \vec{d}(\vec{p}) \cdot \vec{E}_x(t) \exp\left[i \left(\frac{p^2}{2} + I_p \right) t \right]. \tag{2.31}$$

If both the magnitude and phase of this photoionization amplitude are known, the pulse information can be retrieved directly by inverse Fourier transformation. However, only $|b(\vec{v})|^2$ is available experimentally. In order to obtain the phase information, one must rely on the additional information supplied by the laser-assisted photoionization measurement, which

builds the cross-correlation between the XUV pulse and the laser pulse. Our procedure of retrieving the XUV pulse can be described as follows: 1) Using the measured laser-free spectra as input; 2) Starting with a simple guess of the phase of $b(\vec{v})$ to reconstruct the XUV pulse; 3) Use the guessed XUV pulse to calculate laser-assisted photoelectron spectra; 4) Compare the calculated spectra with the measured spectra with the discrepancy recorded as the error function; 5) repeat processes 2) to 4) with another guess until the best (converged) fit was found.

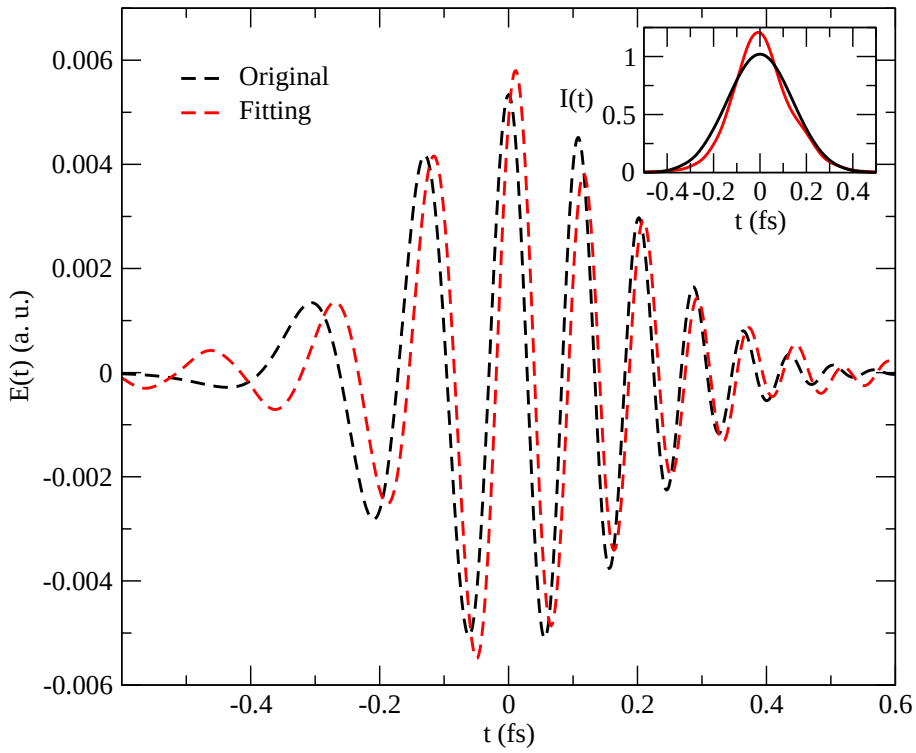

Figure 2.8. Comparison of the retrieved electric field with the original field. The inset shows the intensity profile of the original and the retrieved pulses, in units of 10^{12}W/cm^2.

This fitting process can be improved by using genetic algorithm. To speed up retrieval, instead of comparing the 2D momentum image, we can compare only the trace $E(\theta)$ defined

earlier. In the simplest case, if we assume the XUV pulse is a Gaussian pulse with a linear chirp, then only one parameter must be fitted based on Eq. 2.28.

For the general pulse shape and chirp, we can either discretize the phase into N slices and vary them independently to find the best fit or expand the phase into a polynomial

$$\phi(\omega) = \sum_{i=1}^{N} c_i(\omega - \omega_0)^i \tag{2.32}$$

where ω_0 is the center frequency, and the second order term corresponds to the linear chirp of the pulse. Simulation showed that the latter method converges faster, so this method was used to retrieve the pulse information.

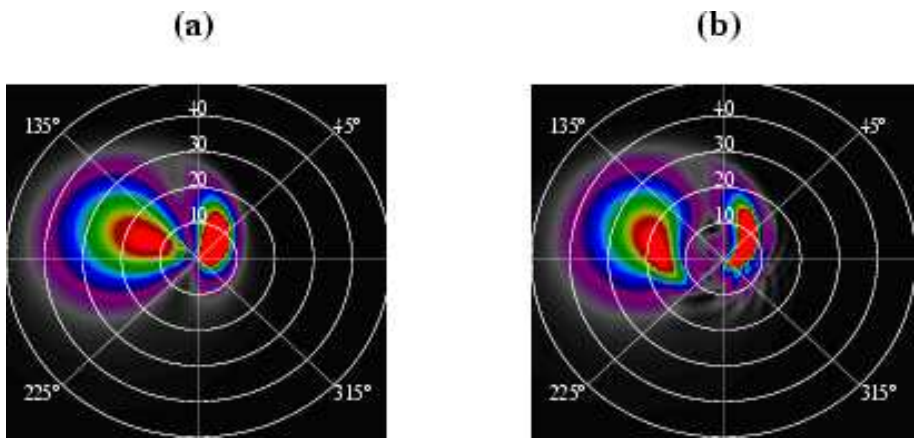

Figure 2.9. Comparison of the photoelectron spectra calculated using (a) the original pulse and (b) the retrieved pulse, at a different time delay of -0.2 fs .

To illustrate the retrieval method, we assumed the measured photoelectron spectrum as given in Fig. 2.5(b). We used the procedure described above to retrieve the XUV pulse information. In the simulation, we chose N=5. The retrieved pulse was compared to the original pulse in Fig. 2.8. Both the magnitude and the phase of the retrieved electric field agreed well. The agreement in the intensity profile was also quite good, as seen in the inset. As a further check on how well the retrieved pulse agreed with the original one, we also

simulated the electron spectrum at time delay of -0.2 fs, using both the original and the retrieved pulses where the first spectrum was supposedly determined experimentally. As shown in Fig. 2.9, the two spectra are in reasonable agreement with each other.

2.5 Conclusions

In summary, we performed calculations of angle-resolved photoelectron spectra of Ar atoms in the combined field of an attosecond XUV pulse and a circularly polarized laser pulse. We examined first theoretically how the electron spectra, including the angular distributions, depended on the pulse duration and the chirp parameter of the XUV light pulse. We also showed how to retrieve or measure the pulse duration and the chirp parameter of such an attosecond XUV pulse if the angle-resolved electron spectra were available from experiments. The method required that the few-cycle lasers be well characterized already, including the carrier envelope phase.

By focusing on the main features of the laser-assisted photoelectron spectra, such as the mean kinetic energy of the photoelectron at a given angle, we showed that it is possible to retrieve the pulse duration and the chirp parameter from the measured electron energy and angular distributions at a given time delay. Systematic checks can be further made through multiple measurements by varying the time delay between the XUV and IR pulses. For attosecond XUV pulses generated by the polarization gating method, the procedure presented in this paper showed be able to characterize the pulse when photoelectron spectra from such cross-correlation measurements become available.

Chapter 3

Laser-dressed autoionization: time-resolved autoionization spectra

3.1 Introduction

Many-electron atomic and molecular systems with excess internal energy relax to states of lower energy by rearranging their electronic structure. With the recently developed attosecond XUV (extreme ultraviolet) pulses [22, 45], it is possible to obtain time-resolved images of an Auger decay [40], akin to the time-resolved spectroscopy for tracking atomic motion in molecules with femtosecond laser pulses [87]. Limited by the pulse intensity, currently, experimentalists employ an XUV pump-IR (infrared) laser probe technique where electrons generated by the XUV pulses are "steered" in the few-cycle IR laser field at varying pump-probe time delays [46, 47]. Although the basic principle of such measurements can be qualitatively understood in terms of classical mechanics, quantitatively, the electron spectra have to be calculated quantum mechanically. For simple laser-assisted photoionization processes, such a quantum theory is readily available by solving the time-dependent Schrödinger equation directly within the one-electron model. However, such calculations are quite tedious and a simpler approximate theory based on the strong field approximation (SFA) [5] has been found [41, 3] to be more useful for analyzing experiments.

In a time-resolved Auger measurement by Dresher *et al.* [40], the Auger electron spectrum in the laser field was analyzed based on an *ad hoc* model that combined a rate equation description of core-hole formation and subsequent quantum theory of Auger emission in the laser field. The theory has been improved recently by Smirnova *et al.* [50], and Wickenhauser and Burgdörfer [88], where the hole formation and the decay process were treated coherently, albeit starting with a somewhat complicated many-electron theory.

In this chapter, we generalize the strong field approximation to calculate the time-resolved electron spectra of an autoionizing state created in a typical XUV pump-IR laser

probe (XUV+IR) experiment. The validity of the SFA thus developed is checked by solving the time dependent Schrödinger equation using a model Hamiltonian that simulates an isolated autoionizing state populated in such XUV+IR experiments. From the simpler SFA theory, we then illustrate how to extract the lifetime of either an isolated resonance or two nearby resonances from the time-domain measurements. We noted that in typical XUV+IR experiments, the attosecond XUV pulse was weak so that the initial autoionizing state is created perturbatively. Thus resonance parameters for characterizing this step were already available from measurements or from many-body calculations in the energy domain. Our starting point was to cast the photoexcitation amplitude in the energy domain into the time domain and then to propagate it in the IR laser field.

3.2 Quantum theory of laser-assisted Autoionization

3.2.1 Laser-dressed decay of a Lorentzian resonance

The energy spectrum amplitude from the decay of a Lorentzian resonance (e.g., Auger decay) can be described by

$$f(E) = -\frac{1}{i(E - Er) - \Gamma/2}, \tag{3.1}$$

where E_r is the center energy of the resonance and Γ is the energy width related with the lifetime of the resonance by $\tau = 1/\Gamma$. The modulus square gives the well-known Lorentzian resonance shape. In a time-dependent picture, the resonance can be considered as a continuous electron emitting process (we focused only on electron emitting). The decay amplitude in time domain is given by the Fourier transformation:

$$F(t) = \exp(-iE_r t - \frac{\Gamma}{2}t) = \int_E dE e^{-iEt} f(E). \tag{3.2}$$

Considering the resonant state populated by an XUV pulse, the photoelectron spectrum can be calculated pertubatively

$$b(\vec{p},t) = i\int_{-\infty}^{t} dt_1 \vec{E}(t_1)\cdot\vec{d}(\vec{p})f(E)e^{iI_p t_1 - iE(t-t_1)}, \tag{3.3}$$

where $\vec{d}$ is the dipole transition moment, and E is the energy of the photoelectron. Inserting the time-dependent decay amplitude, it can be rewritten as

$$b(\vec{p},t) = i\int_{-\infty}^{t} dt_1 \vec{E}(t_1)\cdot\vec{d}e^{iI_p t_1}\int_{t_1}^{t} dt_2 \exp\left[\left(-iE_r - \frac{\Gamma}{2}\right)(t_2-t_1)\right]e^{-iE(t-t_2)}, \tag{3.4}$$

where t_1 is the time that the resonant state is generated and t_2 is the time that decay occurs with the amplitude given in Eq. 3.2. The free propagation of the electron gives the energy phase $e^{-iE(t-t_2)}$.

Now we will generalize the equation to the case where a laser field is accompanying the XUV pulse. Within the strong field approximation, the effect of Coulomb potential and the ionization by the laser field itself is negligible, so the only role the laser field plays is to modify the propagation of the photoelectron. Thus, the energy spectrum of the photoelectron is given by

$$\begin{aligned} b_L(\vec{p},t) = i\int_{-\infty}^{t} dt_1 \int_{t_1}^{t} dt_2 \vec{E}(t_1)\cdot\vec{d}e^{iI_p t_1} \\ \times \exp\left[\left(-iE_r - \frac{\Gamma}{2}\right)(t_2-t_1)\right] \\ \times \exp\{-i\int_{t_2}^{t}\frac{[\vec{p}+\vec{A}(t)-\vec{A}(t_3)]^2}{2}dt_3\}, \end{aligned} \tag{3.5}$$

where $\vec{A}(t)$ is the vector potential related to the electric field by $\vec{E}(t) = -\frac{\partial\vec{A}}{\partial t}$, I_p is the ionization energy, and $\vec{d}$ is the dipole transition moment.

In this formulation, we assumed that the resonant state was populated through dipole transition. It can be modified for the general case by replacing the dipole operator with an appropriate transition operator corresponding to the specific transition. This formula can be understood by considering a virtual three-step process: 1) the resonance state (doubly

excited state or inner shell hole) is excited by XUV pulse at time t_1; 2) the resonant state decays at time t_2 giving birth to a free electron (mathematically we can treat the decay state as a state with complex energy propagating from time t_1 to t_2); 3) the free electron with drift velocity -$A(t_2)$ propagates from t_2 to t. When t goes to ∞, the vector potential vanishes or goes to a constant $A(\infty)$, we have

$$\begin{aligned} b_L(\vec{p}) = i \int_{-\infty}^{\infty} dt_1 \int_{t_1}^{\infty} dt_2 \exp\left[\left(-iE_r - \frac{\Gamma}{2}\right)(t_2 - t_1)\right] \\ \times \exp\{-i \int_{t_2}^{\infty} \frac{[\vec{p} + \vec{A}(\infty) - \vec{A}(t_3)]^2}{2} dt_3\} \\ \vec{E}(t_1) \cdot \vec{d}[\vec{p} + \vec{A}(\infty) - \vec{A}(t_2)] e^{iI_p t_1}. \end{aligned} \tag{3.6}$$

In this model, the IR laser does not participate in the creation of the resonance, and the XUV pulse does not influence the propagation of the continuum electron after its creation. We also assumed that the decay amplitude of the resonant state was not modified by the laser. Thus, the continuum electron is born at time t_2 with momentum $\vec{p'}$, which is related to the momentum $\vec{p}$ at time t when the external field vanishes by $\vec{p'} = \vec{p} + \vec{A}(t) - \vec{A}(t_2)$.

By rearranging the time order of the double integration, the theory presented in the supplementary of [40] by Yakovlev *et al.* can be recovered . The equation above can be rewritten as

$$\begin{aligned} b_L(\vec{p}, \infty) &= i \int_{-\infty}^{\infty} dt_2 \exp\{-i \int_{t_2}^{\infty} \frac{[\vec{p} + \vec{A}(\infty) - \vec{A}(t_3)]^2}{2} dt_3 - iE_r t_2\} \\ &\times \int_{-\infty}^{t_2} dt_1 \vec{E}(t_1) \cdot \vec{d}[\vec{p} + \vec{A}(\infty) - \vec{A}(t_2) \exp\left[-\frac{\Gamma}{2}(t_2 - t_1)\right] e^{i(E_r + I_p)t_1} \\ &\approx i \int_{-\infty}^{\infty} dt_2 \exp\{-i \int_{t_2}^{\infty} \frac{[\vec{p} + \vec{A}(\infty) - \vec{A}(t_3)]^2}{2} dt_3 - iE_r t_2\} \\ &\times \sqrt{\rho(t_2)}\chi, \end{aligned} \tag{3.7}$$

where $\sqrt{\rho(t_2)}$ is the decay amplitude without the phase information and χ represents the transition amplitude to the resonant state, which was induced by the dipole transition in our case.

3.2.2 Fano resonance theory revisited

The total Hamiltonian for a many-electron system can be written in a general form:

$$H = H_0 + V, \tag{3.8}$$

where V is the correlation potential not included in H_0. Suppose we have one doubly excited state located in the continuum of H_0, what we try to do is to find the eigenstate of the full Hamiltonian. Within zero-approximation, the doubly excited state is given by $H_0\phi = E_\phi\phi$, and the continuum is given by $H_0\phi_E = E\phi_E$. Using these orthogonal states as bases, the eigenstate of the full Hamiltonian can be found by solving the equation:

$$H\Psi_E = E\Psi_E. \tag{3.9}$$

The couplings between these states by the full Hamiltonian are given by

$$\begin{aligned} <\phi|H|\phi> &= E_\phi \\ <\phi_{E'}|H|\phi_E> &= E'\delta(E-E') \\ <\phi_{E'}|H|\phi> &= <\phi_{E'}|V|\phi>= V_{E'}. \end{aligned} \tag{3.10}$$

If the states $\phi_{E'}$ are represented by a wavefunction with asymptotic behavior $\sin(k(E')r+\delta)$, after rediagonalizing the Hamitonian matrix, one obtains the eigenstate:

$$\Psi_E = a\phi + \int dE' b_{E'}\phi_{E'}, \tag{3.11}$$

where the coefficients are given by

$$a = \frac{\sin\Delta}{\pi V_E} \tag{3.12}$$

and by

$$b_{E'} = \frac{V_{E'}}{E-E'}a - \cos\Delta\delta(E-E'). \tag{3.13}$$

The phase shift is given by

$$\Delta = -\tan^{-1}\frac{\pi|V_E|^2}{E-E_\phi-F(E)}, \tag{3.14}$$

where

$$F(E) = P \int dE' \frac{|V_{E'}|^2}{E - E'} \tag{3.15}$$

and

$$\Gamma = 2\pi |V_E|^2. \tag{3.16}$$

Substituting $b_{E'}$ into Ψ_E, we have

$$\begin{aligned} \Psi_E &= a\phi + a \int dE' \frac{V_{E'}}{E - E'} \phi_{E'} - \cos\Delta \phi_E \\ &= a\Phi - \cos\Delta \phi_E \\ &= \frac{1}{\pi V_E} \Phi \sin\Delta - \phi_E \cos\Delta, \end{aligned} \tag{3.17}$$

where the modified doubly excited state is given by

$$\Phi = \phi + P \int dE' \frac{V_{E'} \phi_{E'}}{E - E'}. \tag{3.18}$$

If we introduce an operator $\hat{q}$ such that $\frac{1}{\pi V_E}\Phi = \hat{q}\phi_E$, we have

$$\Psi_E = \phi_E(\hat{q} + \epsilon) \sin\Delta, \tag{3.19}$$

where the normalized energy ϵ is defined as

$$\epsilon = \frac{E - E_\phi - F(E)}{\frac{1}{2}\Gamma} = -\cot\Delta. \tag{3.20}$$

The transition probability from an initial state to one of the eigenstates is given by

$$| < \Psi_E|T|i > |^2 = | < \phi_E|T|i > |^2 \frac{(q+\epsilon)^2}{1+\epsilon^2}, \tag{3.21}$$

where q becomes a number. The ratio of the transition probability $| < \Psi_E|T|i > |^2$ to $| < \phi_E|T|i > |^2$ is described by the famous Fano profile:

$$f(E) = \frac{(q+\epsilon)^2}{1+\epsilon^2}. \tag{3.22}$$

Standing wave condition is used in the formulation of the eigenstates Ψ_E above. If incoming wave boundary condition

$$\Psi_E^{(-)}(r) \rightarrow \exp[-i(kr + \delta + \Delta)] \tag{3.23}$$

is applied, where Δ is the eigen-phase shift [89], Ψ_E^- is given by

$$\begin{aligned} \Psi_E^{(-)} &= \phi_E^{(-)}(\hat{q} + \epsilon) \sin \Delta * \exp(-i\Delta) \\ &= \phi_E^{(-)} \frac{\hat{q} + \epsilon}{i - \epsilon}, \end{aligned} \tag{3.24}$$

representing a scattering state. The scattering amplitude from an initial state to one of the scattering states is thus given by

$$< \Psi_E^{(-)}|T|i >= - < \phi_E^{(-)}|T|i > \frac{q + \epsilon}{i + \epsilon}, \tag{3.25}$$

and the q-dependent factor,

$$f_F(E) = \frac{q + \epsilon}{1 - i\epsilon}, \tag{3.26}$$

describes the amplitude of the Fano profile in the energy domain, which can be decomposed into

$$f_F(E) = \frac{q - i}{1 - i\epsilon} + i \equiv (q - i)\frac{\Gamma}{2} f_L(E) + i, \tag{3.27}$$

where $f_L(E)$ is the Lorentzian resonance profile. The modulus square of the q factor gives the same Fano profile in Eq. 3.22.

3.2.3 Laser-assisted autoionization

As discussed in the previous section, an isolated resonance in the energy domain is described by the Fano profile [90], $\frac{(q+\epsilon)^2}{1+\epsilon^2}$, where $\epsilon = \frac{E-E_r}{\frac{\Gamma}{2}}$ is the reduced energy measured from the resonance energy E_r in units of half width $\frac{\Gamma}{2}$. The parameter q measures the relative strength of the formation of the "bound" state and the direct continuum. If the interference between bound and continuum states is small and is neglected, we call it a

Lorentz resonance. In the energy domain, such a resonance is described by the amplitude $1/[i(E-E_r)-\Gamma/2]$. In the time domain, after the Fourier transform, the amplitude decays: $F(t) = \exp(-iE_r t - \frac{\Gamma}{2}t)$. Under the strong field approximation [3] the probability amplitude of finding a continuum electron with momentum $\vec{p}$ at time t after the laser pulse is over is given by Eq. 3.5.

Equation 3.5 can be generalized to an isolated Fano resonance directly. Upon transforming Fano profile given in Eq. 3.27 to the time domain, this would give the amplitude:

$$F_F(t) = \frac{\Gamma}{2}(q-i)e^{-iE_r t - \Gamma t/2} + i\delta(t-0). \tag{3.28}$$

Note that the first term of Eq. 3.28 describes the decay of the "discrete" resonance and the second term describes the prompt photoemission, both in the time-varying electric field of the IR laser. This expression would replace the middle term in Eq. 3.5 in the calculation of electron spectra for a Fano resonance. With a laser present, the first terms gives

$$\frac{\Gamma}{2}(q-i)b_L(\vec{p},t), \tag{3.29}$$

and the the second term gives

$$\begin{aligned} ib_{PI}(\vec{p},t) &= i^2 \int_{-\infty}^{t} dt' \vec{E}(t') \cdot \vec{d}[\vec{p} + \vec{A}(t) - \vec{A}(t')] \\ &\times \exp\left\{ -i \int_{t'}^{t} \frac{[\vec{p} + \vec{A}(t) - \vec{A}(t'')]^2}{2} dt'' + iI_P t' \right\}, \end{aligned} \tag{3.30}$$

where we have assumed that the dipole transition is not modified by the laser field. The sum gives

$$\begin{aligned} b_F(\vec{p},t) &= i \int_{-\infty}^{t} dt_1 \int_{t_1}^{t} dt_2 \vec{E}(t_1) \cdot \vec{d} e^{iI_p t_1} \times \exp\left[-i \int_{t_2}^{t} \frac{(\vec{p} + \vec{A}(t) - \vec{A}(t_3))^2}{2} dt_3 \right] \\ &\times \left\{ \frac{\Gamma}{2}(q-i) \exp\left[\left(-iE_r - \frac{\Gamma}{2} \right)(t_2 - t_1) \right] + i\delta(t2 - t1) \right\}. \end{aligned} \tag{3.31}$$

Clearly this theory reduces to the Fano theory for an isolated resonance in the energy domain in the absence of the IR laser. It also reduces to the SFA theory for laser-assisted

photoionization given by Kitzler *et al.* [43] in the absence of the discrete resonance. Although the derivation is for an autoionizing state, the theory can be applied to describing Auger electron as well if the prompt photoelectrons and the Auger electrons do not interact. We emphasize again that within the SFA, only the field free resonance parameters are used and there is no need to calculate electron spectrum starting from the formidable time-dependent many-electron Schrödinger equation.

3.3 Modeling two-electron systems in laser fields

The theory presented so far is based on the strong field approximation (SFA). The validity of the SFA has been confirmed for laser-assisted photoionization [43] when the photoelectron energy is large compared to the ponderomotive energy of the IR laser field. To see if the present formulation using SFA is indeed valid, we solved the time-dependent Schrödinger equation for a two-electron atom in the XUV + IR field within the two-state approximation and with the same ansatz as in the SFA.

3.3.1 Construction of the two-channel Hamiltonian

Let's start with the Hamiltonian of a two-electron system:

$$H = -\frac{1}{2}\nabla^2_{r_1} - \frac{1}{2}\nabla^2_{r_2} + V(\vec{r}_1, \vec{r}_2). \tag{3.32}$$

Applying the standard adiabatic approximation by choosing $\vec{r}_1$ as the adiabatic parameter, the eigen wave function of this system can be written in the quasi-separable form:

$$\Psi(\vec{r}_1, \vec{r}_2) = \sum_\mu F_\mu(\vec{r}_1)\Phi_\mu(\vec{r}_2), \tag{3.33}$$

where $\Phi_\mu(\vec{r}_2)$ is the channel function satisfying the following Schrödinger equation:

$$\left[-\frac{1}{2}\nabla^2_{r_2} + V(\vec{r}_1, \vec{r}_2)\right]\Phi_\mu(\vec{r}_2) = U_\mu(\vec{r}_1)\Phi_\mu(\vec{r}_2). \tag{3.34}$$

The eigenvalue $U_\mu(\vec{r}_1)$ is the potential surface under which electron 1 is moving. In general, the adiabatic approximation is justified when the motion associated with the adiabatic parameter is slower than the motion of the remaining degrees of freedom. Though it is obviously not true in the system we considered, it won't affect the correctness of the formulation since an infinite complete set of channel functions is implied in this formal theory.

In the presence of an external electromagnetic field $E(t)$, the time-dependent Schrödinger equation (TDSE) is given by

$$i\frac{\partial}{\partial t}\Psi(\vec{r}_1,\vec{r}_2,t) = \left[-\frac{1}{2}\nabla^2_{r_1} - \frac{1}{2}\nabla^2_{r_2} + V(\vec{r}_1,\vec{r}_2) + (\vec{r}_1+\vec{r}_2)\cdot\vec{E}(t)\right]\Psi(\vec{r}_1,\vec{r}_2,t) inthelengthgaugewiththedipole \tag{3.35}$$

Expanding the wavefunction on the set of eigen channels

$$\Psi(\vec{r}_1,\vec{r}_2,t) = \sum_\mu F_\mu(\vec{r}_1,t)\Phi_\mu(\vec{r}_2) \tag{3.36}$$

and substituting it into the TDSE yields close-coupling equations (starting here, $\vec{r}_1$ is denoted as $\vec{r}$)

$$\begin{aligned} i\frac{\partial}{\partial t}F_\nu(\vec{r},t) &= \left[-\frac{1}{2}\nabla^2_r + U_\mu(\vec{r}) + W_{\nu\nu}(\vec{r}) + \vec{r}\cdot\vec{E}(t)\right]F_\nu(\vec{r},t) \\ &+ \sum_{\mu\neq\nu} W_{\nu\mu}F_\mu(\vec{r},t) + \sum_{\mu\neq\nu}\vec{R}_{\nu\mu}\cdot\vec{E}(t)F_\mu(\vec{r},t), \end{aligned} \tag{3.37}$$

where $W_{\nu\mu}$ is the non-adiabatic coupling and $\vec{R}_{\nu\mu}$ is the field-induced coupling of the two channels and given by

$$\vec{R}_{\nu\mu} =< \Phi_\nu|\vec{r}_2|\Phi_\mu > . \tag{3.38}$$

Defining

$$V_\nu = W_{\nu\nu}, \nu = 1,2 \tag{3.39}$$

and

$$V_c = W_{12}, \vec{R}_c = \vec{R}_{12}, \tag{3.40}$$

the TDSE for a model two-channel system is given by

$$\begin{aligned} i\frac{\partial}{\partial t}F_1(\vec{r},t) &= \left[H_1 + \vec{r}\cdot\vec{E}(t)\right] F_1(\vec{r},t) + [V_c + \vec{R}_c\cdot\vec{E}(t)]F_2(\vec{r},t) \\ i\frac{\partial}{\partial t}F_2(\vec{r},t) &= \left[H_2 + \vec{r}\cdot\vec{E}(t)\right] F_2(\vec{r},t) + [V_c + \vec{R}_c\cdot\vec{E}(t)]F_1(\vec{r},t), \end{aligned} \tag{3.41}$$

where

$$H_1 = -\frac{1}{2}\nabla_r^2 + V_1(\vec{r}) \tag{3.42}$$

and

$$H_2 = -\frac{1}{2}\nabla_r^2 + V_2(\vec{r}). \tag{3.43}$$

Rewritten in vector form, the coupled equations are given by

$$i\frac{\partial}{\partial t}\begin{pmatrix} F_1 \\ F_2 \end{pmatrix} = \begin{bmatrix} H_1 & V_c \\ V_c & H_2 \end{bmatrix}\begin{pmatrix} F_1 \\ F_2 \end{pmatrix} + \begin{bmatrix} \vec{r}\cdot\vec{E} & \vec{R}_c\cdot\vec{E} \\ \vec{R}_c\cdot\vec{E} & \vec{r}\cdot\vec{E} \end{bmatrix}\begin{pmatrix} F_1 \\ F_2 \end{pmatrix}. \tag{3.44}$$

In general, the non-adiabatic coupling includes a non-local term (e.g., the kinetic operator). For our purposes we neglect the non-local coupling by assuming V_c is a local potential depending only on $\vec{r}$. The radiation coupling $\vec{R}_c$ depends on the properties of the specific system and should be calculated from the first principle. In order to avoid this complexity in the model, we approximate it as $\vec{R}_c = \vec{r}$ since it has the dimension of a dipole moment. In the simulation, we apply the following assumptions in accord with the analytical model: 1) only one resonant state is concerned; 2) the transition between two channels is through the XUV light. The TDSE is thus approximated by

$$i\frac{\partial}{\partial t}\begin{pmatrix} \psi_1 \\ \psi_2 \end{pmatrix} = \begin{bmatrix} H_1 & V_c \\ V_c & H_2 \end{bmatrix}\begin{pmatrix} \psi_1 \\ \psi_2 \end{pmatrix} + \begin{bmatrix} \vec{r}\cdot\vec{E}_{l+x}(t) & \vec{r}\cdot\vec{E}_x(t) \\ \vec{r}\cdot\vec{E}_x(t) & 0 \end{bmatrix}\begin{pmatrix} \psi_1 \\ \psi_2 \end{pmatrix}. \tag{3.45}$$

Note we use subscripts ℓ and x to indicate electric fields from the laser and the XUV, respectively. This model two-state Hamiltonian is constructed to include the essential ingredients of exciting an autoionizing state in the XUV+IR fields. Without the upper "core" state $\Phi_2(\vec{r}_2)$, the model reduces to a description of laser-assisted photoionization. The coupled

equations are to be solved using partial wave expansion. For definiteness, assume initially $\Phi_1(\vec{r}_1)$ is an s-state. The weak XUV pulse will lead it to p-states only, while the IR laser will couple it to many other angular momentum states via multiphoton processes. In the numerical calculation, following the spirit of SFA, the basis functions for the lower channel include the ground state and the continuum states only. For the upper channel, only one bound eigenstate is included in the basis expansion. This will be a "bound" p-state which is coupled to the ground s-state in the lower channel by the XUV pulse. Once this "bound" p-state is formed it can decay to the continuum p-states of the lower channel through the V_c term, resulting in autoionization as described by Fano [90].

3.3.2 Partial wave expansion

Following the discussion above, the channel wavefunctions are expanded as

$$F_1 = \sum_l f_l(r,t) Y_l(\theta,\phi) \tag{3.46}$$

and

$$F_2 = g_1(r,t) Y_1(\theta,\phi), \tag{3.47}$$

where we have assumed the upper channel only consisting of a p partial wave resonance only. Substituting them into Eq. 3.45, we have

$$i\frac{\partial}{\partial t}\sum_l f_l Y_l(\theta) = H_1 \sum_l f_l Y_l(\theta) + V_c g_1 Y_1(\theta) + \vec{r}\cdot\vec{E}(t)\sum_l f_l Y_l(\theta) + \vec{r}\cdot\vec{E}(t) g_1 Y_1(\theta) \tag{3.48}$$

and

$$i\frac{\partial}{\partial t} g_1 Y_1(\theta) = H_2 g_1 Y_1(\theta) + V_c \sum_l f_l Y_l(\theta) + \vec{r}\cdot\vec{E}(t)\sum_l f_l Y_l(\theta) + \vec{r}\cdot\vec{E}(t) g_1 Y_1(\theta). \tag{3.49}$$

Multiplied by $< Y_{l'}|$ and integrated over the spherical angles, the equations reduce to

$$\begin{aligned} i\frac{\partial f_{l'}}{\partial t} &= \sum_l < Y_{l'}|H_1|Y_l > f_l + V_c g_1 \delta(l',1) + A + B \\ i\frac{\partial g_1}{\partial t} &= < Y_1|H_2|Y_1 > g_1 + V_c f_1 + B', \end{aligned} \tag{3.50}$$

where

$$A = \sum_l f_l < Y_{l'} | \vec{r} \cdot \vec{E}(t) | Y_l >, \tag{3.51}$$

$$B = g_1 < Y_{l'} | \vec{r} \cdot \vec{E}(t) | Y_1 >, \tag{3.52}$$

and

$$B' = \sum_l f_l < Y_1 | \vec{r} \cdot \vec{E}(t) | Y_l > . \tag{3.53}$$

We can see that the coupling V_c operates only on p-partial waves. Term A represents the transition between different partial waves. Terms B and B' represent the coupling between two channels due to the light. Starting from the ground state bounded in the lower channel, resonant state is populated by the XUV light only. Numerical examination shows the effect of laser field on the transition to resonant state is negligible which is consistent with the assumption presented in the analytical model. The reason behind the assumption is that the transition by laser itself requires many more photons, which makes the transition rate much smaller than with the single XUV photon excitation.

3.3.3 Scattering states with incoming wave boundary conditions

In this section, we apply the multi-channel quantum-defect theory [91] to the calculation of scattering states of a two-channel system at the energies that channel 1 is open and channel 2 is closed. In general, there are four linear independent solutions for two coupled second order differential equations at a given energy. Under the boundary condition that the wave functions go to zero when $r \to 0$, only two linear independent solutions exist, i.e., only the regular solutions, satisfying this condition. Note there are two components for each solution, corresponding to channel 1 and channel 2. Our goal is to find the unique solution with a component in the open channel that satisfies the incoming wave boundary conditions,

and a component in the closed channel decaying exponentially, in the asymptotic region. The boundary conditions are given explicitly as

$$\begin{bmatrix} \psi_o^{(-)}(r) \\ \psi_c^{(-)}(r) \end{bmatrix} \rightarrow \begin{bmatrix} i^{-1}(2\pi k_1)^{-\frac{1}{2}}(e^{ik_1 r} - S_o e^{-ik_1 r}) \\ S_c e^{-k_2 r} \end{bmatrix}, \tag{3.54}$$

when $r \rightarrow \infty$, where S_o and S_c are to be determined, subscripts o and c represent open and closed channels, respectively. From the MQDT theory [91], we know that K_o is the scattering matrix (just a number here, $-e^{i\delta}$

The whole configuration space can be divided into inner region ($r \leq R_0$) and outer region ($r \geq R_0$). In the inner region, two linear independent solutions $F_{i\beta}$ can be steadily found by propagating the wave functions from the origin forward to R_0, where i and β indicate the ith channel component of the βth solution. A few propagation methods are available, e.g., Ruga-Kutta method. For sake of numerical ease, the starting point is chosen as a small number r_0 instead of 0 to avoid the singularity at the origin. The two solutions are required to be regular at the origin (r_0), thus the initial conditions for F_β's can be chosen as:

$$\begin{bmatrix} F_{11}(r_0) = 0 & F_{12}(r_0) = 0 \\ F_{21}(r_0) = 0 & F_{22}(r_0) = 0 \end{bmatrix} \tag{3.55}$$

and

$$\begin{bmatrix} F'_{11}(r_0) = r_0^l & F'_{12}(r_0) = 0 \\ F'_{21}(r_0) = 0 & F'_{22}(r_0) = r_0^l \end{bmatrix}, \tag{3.56}$$

where l is the angular momentum of the lth partial wave. Their derivatives are chosen as above because the regular solution is proportional to r^{l+1} for l partial wave in a Coulomb potential. The switch of the initial conditions between solution 1 and 2 is to make them linear independent.

After two linear independent solutions are obtained, the appropriate linear combination of them will give the scattering wave function satisfying incoming wave boundary

conditions. If R_0 is chosen large enough that the coupling is negligible, the wave functions in the outer region coincide with Eq. 3.54. We can simply match the outer wavefunctions to the linear combination of the two inner solutions at R_0:

$$\alpha_1 \begin{bmatrix} F_{11} \\ F_{21} \end{bmatrix} + \alpha_2 \begin{bmatrix} F_{12} \\ F_{22} \end{bmatrix} = \begin{bmatrix} \psi_o^{(-)}(R_0) \\ \psi_c^{(-)}(R_0) \end{bmatrix}. \tag{3.57}$$

Their derivatives need to be matched as well, thus we have four equations to be solved in order to get the four unknowns. Once the unknown are found, the scattering states are obtained in both the inner and outer region by plugging in these coefficients.

Another matching procedure based on [91] is given below. The two linear solutions are matched to the linear combination of energy normalized asymptotic functions at R_0 individually. A linear transformation of the two solutions in the whole space is applied to obtain two new solutions that have outgoing component in a single channel. If both channels are open, we can get all the physical quantity directly from these two solutions. However, since the upper channel is closed, the outgoing component in this channel is not physical. It has exponential growth and decay terms due to the negative energy. The boundary condition for the close channel component are imposed thereafter to eliminate the exponential growth term by making a linear combination of these two solutions, ending up with a unique physical solution.

In both methods mentioned above, the matching distance R_0 must be large enough to ensure that the wave functions are given in the asymptotic form. Because of the exponential growth term, the numerical propagation in the inner region gives very large wave function values at R_0, which makes the accumulated numerical uncertainty too large. In order to control the amplitude of the wave function within the numerical limit, we used a different approach; the wave functions were propagated forward in the inner region and propagated backward in the outer region. In this case, it was no longer necessary to choose a very large R_0.

In the inner region, we used forward propagation to get the two linear independent solutions represented as F_1^a and F_2^a. In the outer region, the wave functions were propagated from a very large distance b (numerically, it could be regarded as infinity) backward to the matching distance R_0. We considered three solutions in the outer region with initial conditions at b as

$$\begin{bmatrix} F_{11}^s \\ F_{21}^s \end{bmatrix} = \begin{bmatrix} ce^{ik_o b} \\ 0 \end{bmatrix}, \begin{bmatrix} F_{12}^s \\ F_{22}^s \end{bmatrix} = \begin{bmatrix} ce^{-ik_o b} \\ 0 \end{bmatrix}, \begin{bmatrix} F_{13}^s \\ F_{23}^s \end{bmatrix} = \begin{bmatrix} 0 \\ e^{-k_c b} \end{bmatrix}; \tag{3.58}$$

$$\begin{bmatrix} F_{11}^{'s} \\ F_{21}^{'s} \end{bmatrix} = \begin{bmatrix} ik_o ce^{ik_o b} \\ 0 \end{bmatrix}, \begin{bmatrix} F_{12}^{'s} \\ F_{22}^{'s} \end{bmatrix} = \begin{bmatrix} -ik_o ce^{-ik_o b} \\ 0 \end{bmatrix}; \tag{3.59}$$

and

$$\begin{bmatrix} F_{12}^{'s} \\ F_{22}^{'s} \end{bmatrix} = \begin{bmatrix} 0 \\ -k_c e^{-k_c b} \end{bmatrix}, \tag{3.60}$$

where c is the energy normalization factor

$$c = i^{-1}(2\pi k_o)^{-\frac{1}{2}} \tag{3.61}$$

with k_o related to the energy by $k_o = \sqrt{2E}$. The physical solutions in the inner and outer region are given by

$$Z^a = \alpha_1 F_1^a + \alpha_2 F_2^a \tag{3.62}$$

and

$$Z^s = F_1^s - K_o F_2^s + K_c F_3^s \tag{3.63}$$

respectively. They are matched at R_c under these matching conditions:

$$\begin{aligned} Z^a(R_c) &= Z^s(R_c) \\ Z^{'a}(R_c) &= Z^{'s}(R_c). \end{aligned} \tag{3.64}$$

Solving this linear system gives the four unknowns $(\alpha_1, \alpha_2, K_o, K_c)$. Therefore, the scattering wave functions satisfying incoming wave boundary conditions are obtained in the whole

space. This method is implemented in the code package ADQF from CPC [92]. We have modified the original code to adapt for photo-absorption processes.

3.3.4 Numerical procedure of solving two-channel time-dependent Schrödinger equation

In the numerical simulation, we performed the following tests to check the reliability of the results.

First, we checked the scattering states to make sure they are calculated correctly and that the photoionization spectrum showed Fano resonance shape. The time-independent Schödinger equations were solved for angular momentum $l = 1$ to get the scattering states

$$|\Psi_E^{(-)}(r) >= M_o^{(-)}(r) + M_c^{(-)}(r) \tag{3.65}$$

with incoming wave boundary conditions for different energies, where o and c denote the open and closed channel component respectively. The reduced transition dipole moment from an initial state $|\psi_g(r) >$ of s-parity to the continuum satisfying incoming wave boundary condition is given by

$$A^{(-)} =< \Psi_E^{(-)}(r)|r|\Psi_g > . \tag{3.66}$$

The photoionization cross section is calculated from the dipole moment using the Fermi Golden rule, showing a Fano resonance shape with parameters depending on the two-channel coupling. Thus, the Fano resonance shape can be readily obtained using this method.

Second, we tested the propagation method and checked to make sure the box size was large enough that non-physical reflection from the boundary did not come into play. The time-dependent Schrödinger equation was solved using the splitting-operator method. Only the interaction of the atom with the XUV pulse was taken into account in this stage. After propagating the initial wave function $|\psi_g(r) >$ to the time when the XUV pulse was off, we projected the final wave function to the scattering states to get the spectrum [93]

shown in Fig. 3.2. The spectrum calculated in this way was consistent with that obtained from the convolution of the cross section with the XUV pulse intensity profile using the perturbation theory.

Finally, we took the laser field into account to examine how the spectrum was changed by the laser field. The wave function is again propagated using split-operator method

$$\psi(r, l, t + dt) = e^{-i\frac{H}{2}dt} e^{-iVdt} e^{-i\frac{H}{2}dt} \psi(r, l, t), \tag{3.67}$$

which is implemented in the pseudo-spectral representation [94, 95] but generalized to two-channel cases. The model system in the combination of XUV and laser pulses were thus solved numerically.

3.4 Time-resolved autoionization spectra

In this section, we first compare the photoelectron spectra of a Fano resonance in the XUV + IR field calculated from the SFA model and the numerical method, and then present time-resolved autoionization spectra calculated using Eq. 3.31. We made a model atom with potentials V_1 and V_2 and their coupling V_c as shown in Fig. 3.1.

The asymptotic energy separation of the two potentials was chosen to be 27.21 eV. With the chosen potentials, the resonance parameters were calculated: E_r=22.9 eV (measured from the first threshold), Γ=0.055 eV (lifetime of 12 fs) and $q = -4.2$. These resonance parameters are used to generate the photoelectron spectra in the strong field approximation using Eq. 3.31. Meanwhile the coupled time-dependent Schrödinger equations for the model atom in the XUV+IR fields are solved numerically to obtain the photoelectron spectra. We assume that the time dependence of both the XUV and that the IR laser pulses are Gaussian and the few-cycle IR laser has a carrier envelope phase ϕ.

In Fig. 3.2, we compare the angle-integrated photoelectron spectra obtained with the following parameters: XUV pulse duration 500 as, central photon energy 39 eV, and

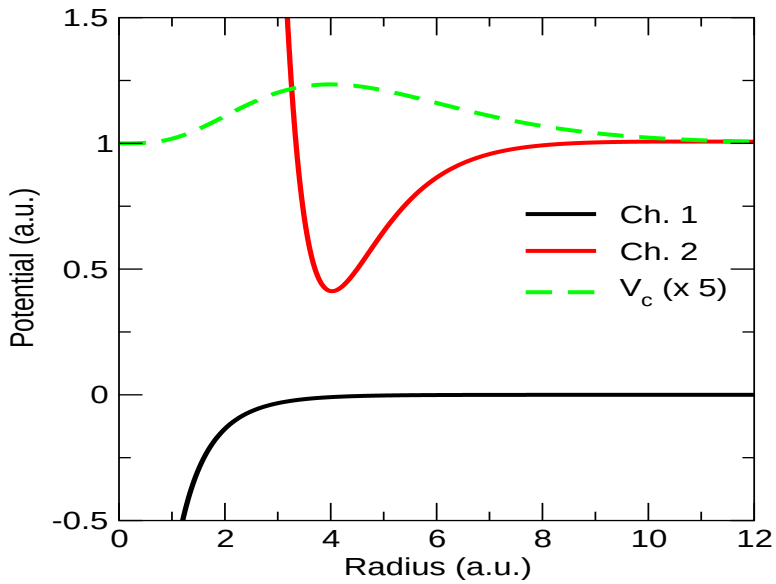

Figure 3.1. Potential curves for a model two-channel system. Black, red and green curves represent V_1, V_2 and V_c respectively. The energy gap between two thresholds is 21.7 eV.

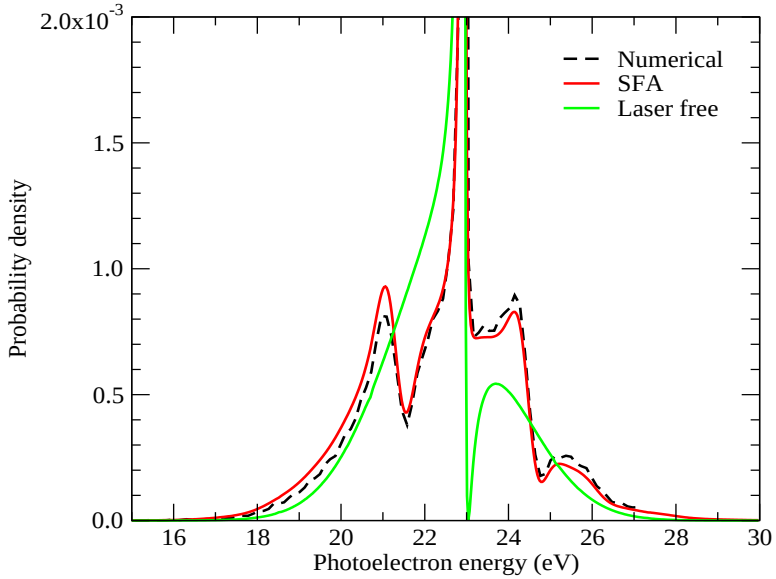

Figure 3.2. Laser-dressed total photoelectron spectrum for an autoionizing state created in XUV+IR laser fields. The spectra from the strong field approximation and from the numerical calculations are shown to agree with each other. The electron spectrum in the absence of lasers is also shown. See text for the parameters used in the calculation.

peak intensity 10^{12} W/cm^2; with a laser duration of 5 fs, the central photon energy is 1.65 eV, peak intensity is 10^{12} W/cm^2, and the carrier envelope phase ϕ=0. The spectra are obtained with no time delay. The comparison shows that the numerical result from the model calculation and from the SFA agree quite well. The Fano profile of the resonance is significantly modified by the laser field and evidences of possible sidebands appear (see later) at 1.65 eV from the resonance on both sides. Other tests show similar general agreement. Thus we will use the SFA model developed here to calculate the electron spectra in XUV+IR experiments.

We next compare the present SFA prediction for the photoelectron spectra in the forward direction with the Auger electron spectra from the recent calculations of Smirnova *et al.* [50], using the same resonance parameters. The XUV has a pulse length of 0.5fs, a mean photon energy of 60 eV and a peak intensity of 10^{12}W/cm^2, while the IR laser has a duration of 6.5 fs, a photon energy of 1.5 eV and a peak intensity of 10^{11}W/cm^2, and ϕ=0. Two Lorentz resonances with lifetimes of (a) 0.2 fs and (b) 2.0 fs, are considered. Figs. 3.3(a) and 3.3(b) shown here are to be compared to their Figs. 2(a) and 2(c), respectively. Although the formation of the resonance is different in the two cases, the dependence of the electron spectra on the laser carrier phase and on the lifetime of the resonance are similar. For the short lifetime resonance, the electron spectrum is broadened significantly. For the longer lifetime state, the sidebands are clearly resolved. In Fig. 3.3 (c) we show the electron spectra in the forward direction for a Fano resonance, with the parameters used in Fig. 3.2 but at different time delays, calculated from the SFA. Electron spectra from the isolated Lorentz resonance part and from the direct photoionization part are shown for each time delay as well. For the Lorentz resonance alone the sidebands are clearly seen. For direct ionization the electron spectrum is broadened and its center shifts with the time delay. The shift stops when the XUV pulse and the IR laser do not overlap in time any more, as shown

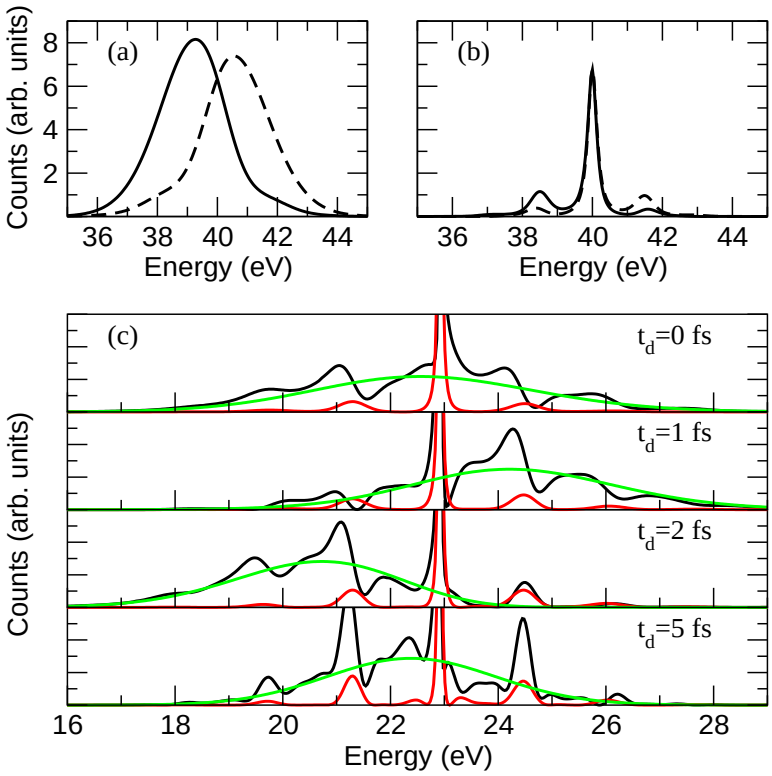

Figure 3.3. Streaked electron spectra in the forward direction for two Lorentz resonances of lifetime of (a) 0.2 fs and (b) 2 fs, excited by a 0.5 fs XUV pulse. The XUV-laser delay time is zero and two carrier envelope phases are shown: 0 (solid) and π (dashed). For other parameters used, see text. (c) Laser modified electron spectra (black) for a Fano resonance at different time delays. Also shown are the electron spectra of the Lorentz resonance alone (red) and the photoionization alone (green). Parameters for the resonance, the XUV and the laser are as in Fig. 3.2 .

for the delay of 5 fs. The total electron spectrum, as the result of interference, appears to be highly "irregular" with respect to electron energy and to the time delay.

Using the present theory, let us analyze the procedure used by Drescher *et al.* [40] for deducing the Auger (or Lorentz resonance) lifetime based on the area of the first sideband for varying time delay between the XUV pulse and the IR laser. In Fig. 3.4 (a) we show the area of the first sideband for electron energy between 20.4 and 22.1 eV versus time delay from -10 fs to 25 fs for a Lorentz resonance represented by the parameters in Fig.3.2

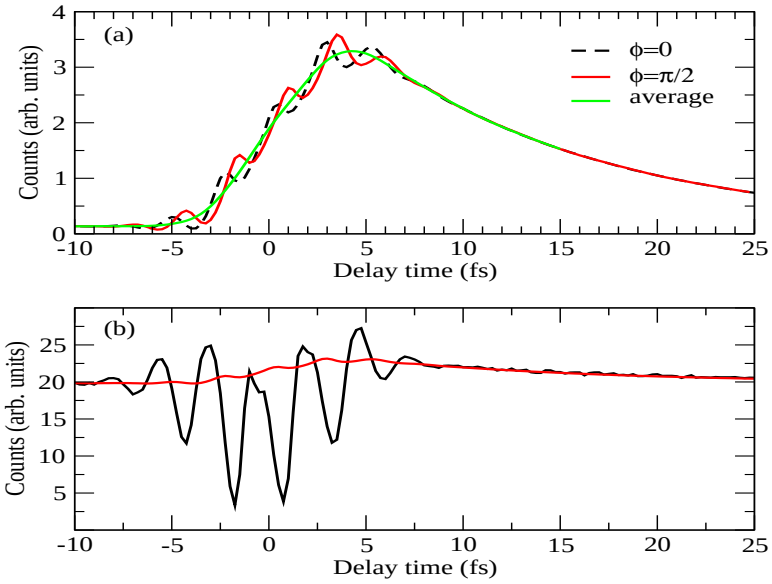

Figure 3.4. (a) Electron counts in the forward direction for a Lorentz resonance within the first sideband [20.4,22.1] eV vs time delay, shown for two carrier envelope phases of the laser and the counts after phase average. (b) Similar electron counts for a Fano resonance for electrons within the energy of [20.4,22.1] eV. The smooth curve gives the counts for the corresponding Lorentz resonance part, except vertically shifted by a constant .

(examples of these sidebands can be seen in Fig. 3.3 (c)). Calculations were shown for two carrier envelope phases: 0 and $\pi/2$. Note that for the small time delay, there is a weak dependence on the carrier envelope phase. For the larger time delay where the XUV and IR pulses do not overlap in time, there is no such phase dependence. On the other hand, by averaging over the carrier envelope phase, a smooth curve is recovered and the result is similar to what was observed by Drescher *et al.* [40]. Note that the modulation in Fig. 3.4 (a) at a smaller time delay is separated by 2.5 fs –the period of the IR laser.

Can the lifetime of a Fano resonance be extracted in a similar manner in view of the fact that the electron spectra, with respect to the time delay, as seen in Fig. 3.3 (c), do not show any clear sidebands? In Fig. 3.4 (b), we show the electron counts within the interval [20.4, 22.1] eV, as in the isolated Lorentz resonance, versus the time delay. For small

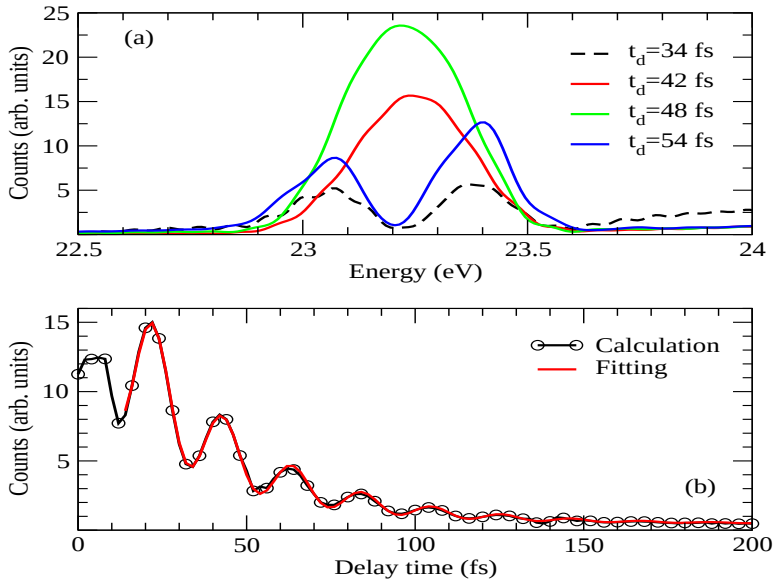

Figure 3.5. (a) Streaked electron spectra within the first sideband vs time delay for two nearby Lorentz resonances excited by an attosecond pulse. (b) The oscillatory total electron counts within the sideband vs time delay can be fitted to extract the lifetimes of the two resonances and their energy separation, see text .

time delays, there are large oscillations. But for long time delays, the oscillation becomes weaker. In Fig. 3.4 (b), the smooth line is from the Lorentz resonance part alone, except when shifted by a constant. This clearly shows that interference from the direct ionization is small at large time delays and the smooth curve can be fitted by an exponential law $\exp(-\Gamma t_d)$ (t_d is the time delay), from which the lifetime of the resonance is extracted. In fact in such an analysis we have tested that the extracted lifetime is independent of the specific selection of the energy bins used for the total electron counts.

The present formulation can be easily extended to obtain electron spectra for two nearby resonances. Consider two Lorentz resonances at 24.8 eV and 25.0 eV, with lifetimes of 30 fs and 40 fs, respectively, created by a 0.5fs XUV pulse at a peak intensity of 10^{12} W/cm^2 into an IR laser of 10 fs, a frequency at 1.65 eV and a peak intensity of 10^{12} W/cm^2. The streaked electrons from the two resonances will interfere. In Fig. 3.5 (a) we show the

spectra near the first sideband versus the time delay. One can see clearly that the electron spectrum shows oscillations within the sideband. The total electron counts within (22.4, 24.0) eV versus the time delay are shown in Fig. 3.5 (b). The damped oscillations can be fitted by $c_1 e^{-\Gamma_1 t_d} + c_2 e^{-\Gamma_2 t_d} + c_{12} e^{-(\Gamma_1+\Gamma_2)t_d/2} \cos(\Delta E t_d + \phi_0)$, where t_d is the time delay, from which one can extract the two lifetimes and the energy separation ΔE between the two resonances. (Note: The line in the figure was fitted with the two given lifetimes and the input energy separation.)

In summary, we have presented a quantum theory for describing the photoelectron spectra of an autoionizing state created by an attosecond XUV pulse in the streaked few-cycle IR laser field within the strong field approximation that is expected to form the basis of future time-resolved experiments on resonances with attosecond pulses. We illustrated the utility of the theory by extracting the lifetime of an isolated and two nearby resonances from the time-resolved electron spectra. Future work may involve the possibility of extracting the q parameter of a Fano resonance and applications to more resonances. We comment that no real strong field effects are included in the present theory. For higher IR laser powers, one may expect new resonances to appear, similar to the new resonances induced by the static electric field [96]. In such cases, there is no clear alternative but to develop a real time-dependent many-electron theory.

Chapter 4

Alignment-dependent ionization of diatomic molecules

4.1 Introduction

In the past few decades, much interest has been devoted to exploring the nonperturbative interaction between molecules and intense lasers. Problems of basic scientific and practical importance include the orientation, steering and focusing of molecular beams [97, 98, 99]. In particular, the ionization of molecules by short pulse lasers may be used as soft ionizer [100] for large molecules and for efficient high-order harmonic generation (HHG) into the soft X-ray region [101]. Further development of these and other applications of intense lasers to manipulate molecules requires a solid theoretical foundation for understanding the detailed dynamics of molecules in strong laser fields. While several simple theoretical models [5, 77, 78, 6] have been successfully employed to interpret the ionization of atoms in intense laser fields, these models have limited usefulness for molecules.

Unlike atoms, molecules are not isotropic systems, and it is clear that the ionization rate can be strongly influenced by the alignment angle θ between the molecular axis and the laser electric field vector. Since the rotation period of a typical molecule (a few ps) is much longer than the pulse duration (100 fs or less) of Ti:Sapphire lasers, each ionization can be considered to occur for a molecule fixed in space. The ionization rate of such an aligned molecule in a laser field can be calculated in principle as for atoms, but few calculations have been done [102, 103] because of computational complexities. To achieve a general understanding of laser-molecule interactions we thus developed a molecular tunneling ionization model for calculating the ionization rate of molecules in an intense laser field [104]. This model is an extension of the ADK (Ammosov-Delone-Krainov) model [6] for atoms, which has been successfully used for describing the ionization rate of an atom in the tunneling ionization regime. The MO-ADK model has been used to calculate the

ionization rates for molecules and the results have shown good agreement with experimental data [55, 56, 58, 59]. The MO-ADK model also has successfully interpreted the origin of the so-called ionization suppression for some molecules [104]. In order to compare with experiments, the ionization rates predicted by the MO-ADK model have to be averaged over an ensemble of randomly distributed molecules. Thus, the alignment dependence of the ionization rate is not tested directly. In this chapter, we discuss the determination of such alignment dependence in a double-pulse experiment.

We started with a short pump laser and waited for the molecules to be aligned at a later time (a few picoseconds) when they undergo "rotational revival" [105, 106]. During this interval, which lasts for a few hundred femtoseconds, the degree of alignment of the molecules changes rapidly. A second short probe laser is used to ionize these aligned molecules, and the ionization yield can be measured against the delay time between the two pulses. The short pulses are used to better align the molecules during free propagation after the field. Within this limit, the effect of the laser field on the rotation of the molecule can be described by the rigid rotor model[107, 106, 108, 109]. Within this model, the alignment of the molecules in the laser field can be calculated using quantum mechanics, but the effect can also be understood by treating the rotor motion classically. The angular distribution of molecular axes can be determined by Coulomb exploding the molecules [62, 63]. MO-ADK model is thus tested from the alignment dependent ionization rates of molecules. On the other hand, the alignment dependent ionization rates provide information about the molecular structure. By examining the differences in ionization of N_2 and O_2 molecules, the role of the valence electron orbital is identified.

In this chapter, we will first discuss the theory for field-free alignment and rotational revival of molecules, then briefly discuss the MO-ADK theory, and present the alignment-dependent ionization rates for diatomic molecules N_2 and O_2. Finally, we discuss the pump-probe experiment for determining the alignment dependence of ionization rates.

4.2 Alignment of molecules by lasers: The classical rotor model

The complete description of molecules in laser fields involves the coupling of lasers with the different degrees of freedom of molecules: electronic motion, vibrational motion, and rotational motion (translation motion and spin freedom are not explicitly considered). The time scales associated with each of these motions are quite different, roughly about attoseconds for the electronic motion, femtoseconds for the vibrationl motion, and picoseconds for the rotation motion. Therefore in general, these motions are weakly coupled. If we are only focusing on the rotation of molecules in a weak laser field, we can neglect all the other degrees of freedom, i.e., assuming no ionization, no electronic and no vibrational excitation, and thus the molecules are modeled as rigid bodies, or rigid rotors for diatomic molecules. The dipole moment of a molecule in a weak static electric field is given by

$$\vec{\mu} = \vec{\mu}_0 + \frac{1}{2}\vec{\vec{\alpha}}\vec{E} \tag{4.1}$$

where μ_0 is the permanent dipole moment that is zero for homonuclear diatomic molecules. The second term is from the induced dipole moment by the field. Higher order terms are usually weaker and can be neglected. Here α is the anisotropic polarizability tensor of the molecular electronic ground state with two principal components $\alpha_\parallel$ and $\alpha_\perp$, parallel and perpendicular to the molecular axis, respectively. (Note that the definition of polarizability can differ by a factor of 1/2 in some literatures.) The induced dipole moment is explicitly given by

$$\frac{1}{2}\vec{\vec{\alpha}}\vec{E} = \frac{1}{2}[\alpha_\parallel E\cos\theta\hat{e}_\parallel - \alpha_\perp E\sin\theta\hat{e}_\perp] \tag{4.2}$$

in the body frame, where θ is the angle of the molecular axis with respect to the electric field and $\hat{e}_\parallel$ and $\hat{e}_\perp$ represent, respectively, the direction parallel and perpendicular to the molecular axis. The electric field vector is given in the body frame by

$$\vec{E} = E\cos\theta\hat{e}_\parallel - E\sin\theta\hat{e}_\perp. \tag{4.3}$$

For molecules in a weak linearly polarized laser field, assuming that the polarizability is the same as that in a static field, the classical rotational motion is governed by Newton's equation:

$$I\frac{d^2\theta}{dt^2} = \vec{\mu} \times \vec{E}(t) \tag{4.4}$$

where I is the moment of inertia of the molecule and is related to the rotational constant by $B = \frac{1}{2I}$. The torque exerted on the molecules is given by

$$\vec{\mu} \times \vec{E}(t) = \mu_0 E(t) \sin\theta - \frac{1}{4}\alpha E^2(t) \sin 2\theta \tag{4.5}$$

with $\alpha = \alpha_{\parallel} - \alpha_{\perp}$ determined by the anisotropic polarizability of the molecules.

4.3 Adiabatic alignment

4.3.1 Classical description

Considering a laser field with optical period (2.7 fs for typical Ti-Sapphire laser field) much shorter than the rotational period, the equation of motion averaged over a laser cycle (from Eq. 4.4 and Eq. 4.5), reduces to

$$\frac{d^2\theta}{dt^2} = -\frac{\alpha E_0^2}{8I} \sin 2\theta. \tag{4.6}$$

This is an equation describing the motion of a pendulum. Note the permanent dipole term vanishes after averaging over one cycle. Applying small angle approximation, the equation reduces to

$$\frac{d^2\theta}{dt^2} = -\frac{\alpha E_0^2}{4I}\theta \equiv -\omega_p^2\theta \tag{4.7}$$

where ω_p is the pendular frequency. Under this approximation, all molecules in the ensemble rotate at the same frequency and oscillate around the laser polarization direction. In this case, the alignment time might be defined as one quarter of the period of the pendular motion [105]. For N_2 molecules (rotational constant 2 cm^{-1}) in a laser field of intensity

2.5×10^{12} W/cm^2, the alignment time is about 400 fs. For molecules in a pulse, averaging over laser cycles can still be performed to simplify the calculation when the pulse duration is much longer than the laser period, which ends up with the pendulum equation depending only on the field intensity profile [110]. However, this approximation does not hold for ultrashort laser pulses and the equation has to be solved numerically without averaging over the cycles [111]. By examining the trajectories of the angle between the molecular axis and the laser polarization direction, it was found [111] that as the laser intensity increases, the torque exerted on the molecule begins to cause reorientation; further increase in intensity leads to ionization, bond stretching and multiple ionization which are not taken into account in the rigid rotor model. If the laser field is high enough, oscillation about the polarization direction happens. However, for longer pulses, the oscillation amplitude is very small showing adiabatic alignment. In order to take the initial random orientation of molecules into account, a Monte-Carlo-like simulation will be necessary. We will not discuss this since the ensemble effect can be best investigated quantum mechanically as described below.

4.3.2 Quantum mechanical treatment: Pendular States

The Schrödinger equation for a linear rotor in a laser field $E(t) = E_0 \cos \omega t$ with duration τ_p is given by

$$[B\hat{J}^2 + V_\mu(\theta) + V_\alpha(\theta)]\psi(\theta, \phi) = \epsilon\psi(\theta, \phi) \tag{4.8}$$

where B is the rotational constant $\frac{1}{2I}$ and where

$$V_\mu(\theta) = -\mu_0 E(t) \cos\theta \tag{4.9}$$

$$V_\alpha(\theta) = -\frac{E^2}{2}(\alpha_\parallel \cos^2\theta + \alpha_\perp \sin^2\theta) \tag{4.10}$$

are the interactions of the laser field with the permanent and induced dipole moments. This effective Hamiltonian can also be derived from the full Hamiltonian by approximately

averaging over the faster vibrational motion, the electronic motion and the rotation. In the long pulse limit ($\omega \gg \frac{1}{\tau_p}$), averaging over cycles gives

$$[B\hat{J}^2 - \frac{E^2}{4}(\alpha_{\parallel}\cos^2\theta + \alpha_{\perp}\sin^2\theta)]\psi(\theta,\phi) = \epsilon\psi(\theta,\phi) \tag{4.11}$$

When the laser field goes to zero, it describes a field-free rotor, and when the field goes to infinity, it describes a 2-dimensional liberator. The eigenstates thus can be labelled by $|M|$ and energies that correlate adiabatically to the field free rotational states in the low field limit and to the liberator states in the high field limit. The alignment parameter, measured by $\cos^2\theta$, for the pendular states can be evaluated as shown in [112, 113]. Starting from one of the field free rotational states, the wavefunction will adiabatically evolve to a pendular state that depends on the laser intensity. The degree of alignment depends on which pendular state it will reach. The pendular state is not an eigenstate of the free rotor. Instead, it is a superposition of the field-free rotational states. In order to align a molecule initially from one of the rotational states, excitation to other states must occur to get the appropriate coherent superposition of rotational states to construct a pendular state. In other words, the interference between different rotational states is important in aligning molecules.

4.4 Dynamic alignment

4.4.1 Kick model and field-free alignment

The time-dependent Schödinger equation describing a rotor in a linearly polarized laser pulse is given by

$$i\frac{\partial\psi(\theta,\phi,t)}{\partial t} = [B\hat{J}^2 + V_{\alpha}(\theta,t)]\psi(\theta,\phi,t).$$

Here we consider only laser fields with far-off resonance frequencies (no laser induced resonant excitation), and the permanent dipole term is neglected, assuming the laser frequency

is much larger than the rotational frequency. The magnetic quantum number m is conserved in this process. Only even or odd rotational states (depending on the initial state) are excited through the induced dipole interaction.

When the pulse is much longer than the rotational period, i.e., in the adiabatic limit, this equation reduces to that of the laser-induced pendular motion studied in the previous section. If the pulse is much shorter than the rotational period, the interaction can be considered as an impulse and treated by the so-called kick model. Assuming the molecular axis is frozen within the duration of the short pulse (much less than the rotational period), we can neglect the kinetic energy part on the right. The wavefunction at the time of the kick is given by

$$\psi(\tau_p) = \exp(-i \int_0^{\tau_p} V_\alpha(\theta, t)dt)|\psi(0) >= \sum_J C_J |JM >, \tag{4.12}$$

which has been expanded in terms of field-free rotational states. After the pulse is turned off, the molecular wavefunction continues to propagate in the free space,

$$\psi(t + \tau_p) = \sum_J C_J e^{-iBJ(J+1)t} |JM > . \tag{4.13}$$

Between the adiabatic and impulsive limits, the time-dependent Schödinger equation has to be solved numerically. In the simulation, the TDSE is solved independently for each individual initial rotational state $|JM >$ (up to $J = 40$) using the split-operator method [94, 95]. Assuming the Boltzman distribution of the rotational levels at the initial time, the alignment parameter at a given temperature is defined by

$$< \cos^2\theta >= \sum_J w_J \sum_{M=-J}^{M=J} < \cos^2\theta >_{JM}, \tag{4.14}$$

where the ensemble average has been taken and w_J is the Boltzman factor. This measures the degree of alignment and has a value of $\frac{1}{3}$ for a randomly distributed molecular ensemble.

For homo-nuclear diatomic molecules, statistics of nuclei spin must be taken into account as well. The total wavefunction of a molecule can be written as

$$\Psi_{total} = \Psi_{electron}(R, \vec{r})\Psi_{rotation}\Psi_{nuclearspin}. \tag{4.15}$$

If the two nuclei are bosons of spin I, the total wavefunction should be symmetric under the exchange of the two nuclei. Among the $(2I+1)^2$ degeneracy of the nuclei spin, $(2I+1)(I+1)$ are symmetric and $(2I+1)I$ are antisymmetric. The rotational partition function can thus be written as $g_g Z_g + g_u Z_u$, where g_g and g_u are the statistics factors for symmetric and antisymmetric nuclear spin states respectively and given by

$$g_g = \frac{i+1}{2i+1}, g_u = \frac{i}{2i+1}. \tag{4.16}$$

The associated partition functions Z_g and Z_u are only for even or odd rotational states depending on the statistics of the nuclei spin and the symmetry of the molecules. The symmetry property of the rotational wavefunctions is that they are symmetric for even J and antisymmetric for odd J, For the electronic wavefunction, the interchange of the two nuclei amounts to change $\vec{R}$ to $-\vec{R}$. This change is even for Σ_g^+ and Σ_u^- and odd for Σ_g^- and Σ_u^+. Thus for $^{16}O_2$ which has a $^3\Sigma_g^-$ ground state and $I = 0$, even J will go with antisymmetric nuclei spin states with weight 0 and odd J go with symmetric nuclear spin state with weight 1. Thus all the even J rotational states are missing. For H_2, a similar argument shows that even even J has a weight of 1 and odd J has a weight of 3.

As an example, Fig. 4.1 illustrates how the alignment parameter of oxygen molecules changes with time based on numerically solving TDSE. Within the pulse duration, the molecules achieve little alignment, which means essentially that the molecule just experiences a kick. The kick imparts a rotational angular momentum to each molecule. Thus, even after the kick is over, the molecules continue to rotate until the alignment reaches a maximum. After the maximum alignment, the continual rotation of the molecules reduces

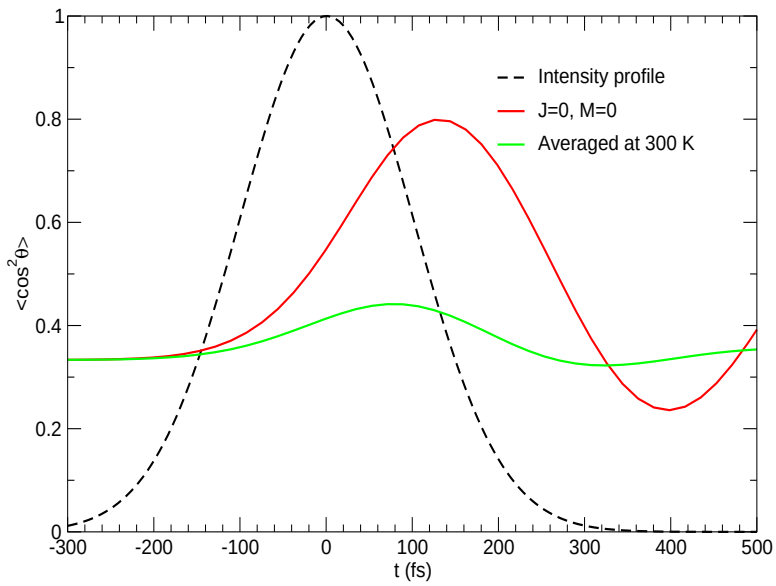

Figure 4.1. Alignment of N_2 molecules by a laser pulse with intensity 2×10^{13} W/cm^2, duration 250 fs. Dashed line depicts the laser intensity profile. Red line shows the alignment parameter $< \cos^2\theta >$ for N_2 molecule initially in J=0 rotational state. Green lines shows the thermal averaged alignment parameter at room temperature 300 K.

the degree of alignment until they reach further alignment at periods of rotational revival. Such rotational revival is seen for both individual initial rotational states and for the thermally distributed ensemble of molecules. This phenomenon of field-free alignment can be explained qualitatively, either from classical or quantum mechanical point of view, and has been first addressed in [106].

According to classical mechanics, we consider an ensemble where all the molecules are randomly aligned before the kick. The amount of angular momentum transferred to the molecule by the kick can be calculated from the torque, which is the derivative of the interaction potential. Torque is given by

$$\Delta J_{transfer} \propto -\sin 2\theta, \tag{4.17}$$

suggesting that molecules initially at larger angles get higher angular momentum transferred and thus would start rotating faster. Later, they will catch up with those molecules, initially

at the smaller angles, and thus localization of the density occurs and maximum alignment is achieved. Afterwards, the molecules keep rotating with different velocities and the alignment is destroyed.

From the viewpoint of quantum mechanics, narrow angular alignment requires a broad distribution of rotational angular momenta from the kick. However, broad distribution does not necessarily gives narrow angular distribution. They have to interfere constructively. After the pulse, the wave packet keeps evolving freely. The phases of different rotational components are proportional to the product of the rotational energy and time. Because the rotational energies for different angular momentum components are quantized, the phases from the different components add coherently at the time of rotational period T of the molecule. The alignment of molecules at these times is said to undergo full rotational revival. Quarter- and half-revival also occur at T/4, T/2, 3T/4, etc. For other times, the phases from different rotational components interfere more randomly, and the molecules lose alignment.

In the language of optics, the rotational wave packet is chirped by the kick. It is similar to the optical interference from a grating. In order to narrow the angular distribution, the chirp need to be compensated. The analogy in optics is to compress a chirped pulse. In order to compensate the chirp, light is sent to pass through a dispersive medium like a piece of glass. In the case of rotational revival, free propagation is naturally dispersive, because the energy factor for each rotational component J is proportional to $J(J+1)$. After a certain time, the phases are compensated to give maximum alignment. From this point of view, the control of rotational wave packet is analogous to controlling a pulse, which leads to possible quantum information processings [114].

A larger kick is desired in order to best aligning the molecules during the post-pulse propagation. Because ionization will destroy the molecules, we want to keep the ionization rate small while giving a larger kick. This leaves only one option: increasing the pulse

duration. However, if the pulse is too long, the kick model fails. The molecules are pushed adiabatically to one of the pendular states in the laser field and thus return to the original field-free rotational state upon the adiabatic turn-off of the laser field. The alignment will vanish after the pulse is over. Therefore, an optimal pulse duration distinguishing the kick and the push limits exists for a given laser intensity. Take the pulse intensity of 2×10^{13} W/cm^2 with pulse duration of 250 fs. From the MO-ADK theory, we calculated that the ionization probability for such a pulse is less than 10^{-10} for N_2 and less than 10^{-8} for O_2.

By varying the duration of the pulse, and solving the TDSE numerically, the degree of alignment versus the pulse duration is obtained and optimal pulse duration can be found. Fig. 4.2 shows how the alignment depends on the pulse duration for N_2 and O_2 molecules at a variety of temperatures. Clearly the molecules are better aligned at lower temperatures. In the plot, the alignment is more prominent at 25 K. For a pulse shorter than the optimal duration, the alignment is increased monochromatically with pulse duration suggesting that the laser-molecule interaction can be treated as a kick. The optimal pulse duration is related to the rotational constant of molecules. It is found that the optimal pulse duration is 300 fs for O_2 molecules and 250 fs for N_2 molecules, assuming that no ionization occurs.

4.4.2 Field-free rotational revival and partial revival

After the pulse ends, the rotational wave packet propagates freely. Though the probability of the projection on different rotational components is constant, the phase varies linearly with time. Because the energies of different rotational components are integer multiples of $2B$, i.e., $E_J = BJ(J+1)$, after the pulse, the wavefunction repeats itself periodically with a revival time

$$T_r = \frac{\pi}{B}, \tag{4.18}$$

where the alignment parameter also reaches its maximum periodically. However, detailed study on the alignment parameter reveals more structures [63].

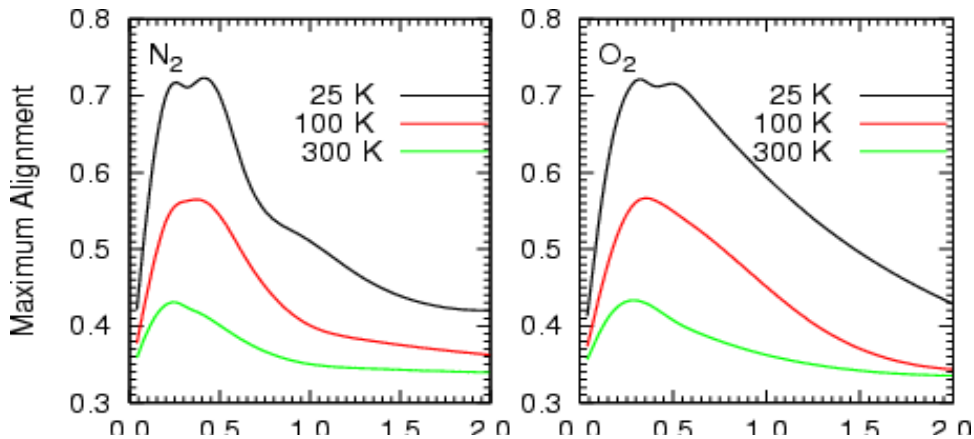

Figure 4.2. ; at a peak intens cated in the plot.

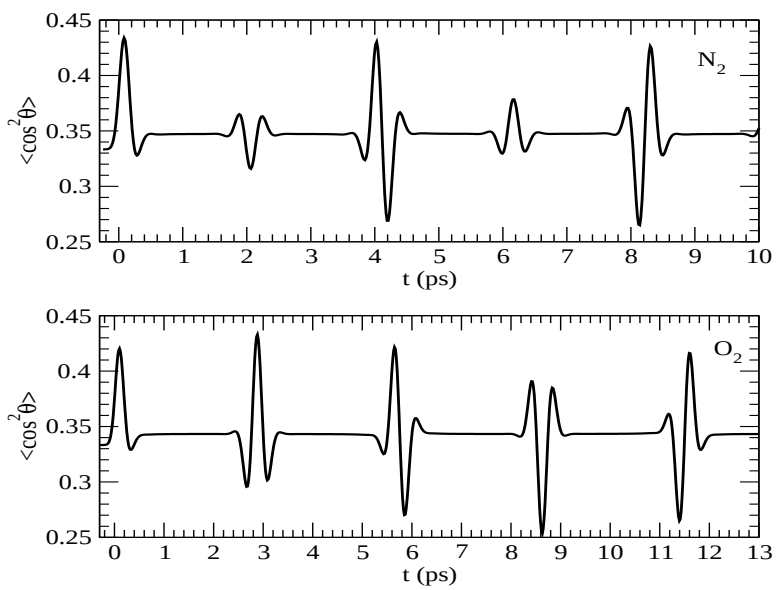

Figure 4.3. Alignment parameter $< \cos^2\theta >$ of N_2 and O_2 molecules at temperature 300K vs time after pumped by a laser pulse with intensity 2×10^{13} W/cm^2 and duration 250 fs.

Figure. 4.3 shows how the calculated alignment parameters change with time for N_2 and O_2 molecules at room temperature 300 K. The revival period T_r is about 8 ps for N_2 and 12 ps for O_2. However at half and quarter period, the alignment parameter shows partial revival, especially the alignment is reversed at half period [108, 115]. The partial revival phenomena are explained in the following discussion.

From the expansion of the wavefunction, the alignment parameter is given by

$$< \psi| \cos^2\theta|\psi >= \frac{1}{3} + \frac{1}{3}\sqrt{\frac{16\pi}{5}} \sum_{J,J'} C_J^* C_{J'} e^{-i\Delta E_{JJ'}t} < JM|Y_{20}|J'M > . \tag{4.19}$$

The coupling matrix element of the second term on the right is nonzero only when $J' - J = \pm 2$ due to the symmetry property of operator Y_{20}. The interference between J and J' states gives the time-dependent phase factor

$$\cos[-Bt[(J+2)(J+3) - J(J+1)] + \phi] = \cos[-2B(2J+3)t + \phi]. \tag{4.20}$$

Experimentally, the distribution of the rotational states, or the beat frequencies between different states have been explored from the transformation of the alignment parameter which is measured by Coulomb exploding the molecules [63]. The observed beat frequencies show direct evidence of Eq. 4.20.

Because the rotational states with even and odd parities mix up due to the statistics, the calculation of alignment parameter for the whole ensemble can be separated into two parts:

$$g_g Z_g < \cos^2\theta >_g, g_u Z_u < \cos^2\theta >_u . \tag{4.21}$$

Whenever the time is multiples of T_r, the alignment parameter repeats itself giving full revival of alignment. At time $\frac{T_r}{2}$, $\cos[-2B(2J+3)t + \phi]$ changes its sign for both even and odd symmetry rotational ensembles, maximum and minimum switches, reversed revival is obtained. At time $\frac{T_r}{4}$, the phase factors $\cos[-2B(2J+3)t + \phi]$ for the sub-ensemble g and u are opposite signs. If the average of Y_{20} for the two sub-ensembles are approximately

equal (a good approximation for ensembles at high temperature), the alignment parameter is given by

$$\frac{1}{3} + \frac{1}{3}\sqrt{\frac{16\pi}{5}}\frac{g_g Z_g - g_u Z_u}{g_g Z_g + g_u Z_u} < Y_{20} > \tag{4.22}$$

or

$$\frac{1}{3} + \frac{1}{3}\sqrt{\frac{16\pi}{5}}\frac{g_g - g_u}{g_g + g_u} < Y_{20} > \tag{4.23}$$

at high temperature assuming $Z_g = Z_u$. If the statistical factors g_g and g_u give equal weight, then partial revival will disappear. For N_2 molecules, the degree of partial revival alignment at $\frac{T_r}{4}$ and $\frac{3}{4}T_r$ is only $\frac{1}{3}$ of that at full revival time. For O_2 molecules, no even J rotational states, the degree of alignment at $\frac{T_r}{4}$ and $\frac{3}{4}T_r$ has the same order of that at the full revival time.

4.5 Molecular tunneling ionization theory

The ADK theory for ionization of atoms in a laser field is based on the tunneling of an electron through the suppressed potential barrier of the combined atomic field and the external electric field. For a static electric field and for a hydrogenic atom the tunneling rate can be calculated analytically. The ADK theory is obtained by modifying the analytical formula by considering nonhydrogenic atoms. The chief among them is the modification of the radial wave function of the outermost electron in the asymptotic region where tunneling occurs. To obtain tunneling ionization rates for molecules, similar considerations on the electronic wave functions in the asymptotic region have to be considered. The ADK model for atoms was derived for an electronic state that initially has a well-defined spherical harmonics. To employ analytical expressions for the ionization rates for molecules, one has to express the molecular electronic wave functions in the asymptotic region in terms of summations of spherical harmonics in a one-center expansion. In the molecular frame, the

asymptotic wave function of a valence electron in a diatomic molecule at large distances can be expressed as (recall that atomic units $m = \hbar = e = 1$ are used)

$$\Psi^m(\vec{r}) = \sum_l C_l F_l(r) Y_{lm}(\hat{r}), \tag{4.24}$$

with m being the magnetic quantum number along the molecular axis. We normalize the coefficient C_l in such a way that the wave function in the asymptotic region can be expressed as

$$F_l(r \to \infty) \approx r^{Z_c/\kappa - 1} e^{-\kappa r}, \tag{4.25}$$

with Z_c being the effective Coulomb charge, $\kappa = \sqrt{2I_p}$, and I_p being the ionization potential for the given valence orbital. Here, we assume that the molecular axis is aligned along the external field direction. The valence electron will be ionized along the field direction at $\theta \approx 0$. The leading term of the spherical harmonic along this direction is

$$Y_{lm}(\hat{r}) \simeq Q(l,m) \frac{1}{2^{|m|}|m|!} \sin^{|m|}\theta \frac{e^{im\phi}}{\sqrt{2\pi}}, \tag{4.26}$$

with

$$Q(l,m) = (-1)^m \sqrt{\frac{(2l+1)(l+|m|)!}{2(l-|m|)!}}. \tag{4.27}$$

The wave function in the tunneling region can be written as

$$\Psi^m(\vec{r}) \simeq B(m) r^{Z_c/\kappa - 1} e^{-\kappa r} 2^{|m|} |m|! \sin^{|m|}\theta \frac{e^{im\phi}}{\sqrt{2\pi}} \tag{4.28}$$

with

$$B(m) = \sum_l C_{lm} (-1)^m \sqrt{\frac{(2l+1)(l+|m|)!}{2(l-|m|)!}}. \tag{4.29}$$

Following the same procedure used in [116], we obtain the ionization rate of a diatomic molecule in a parallel static electric field as

$$\begin{aligned} w_{stat}(F) &= \frac{B^2(m)}{2^{|m|}|m|!} \frac{1}{\kappa^{2Z_c/\kappa - 1}} \\ &\times \left(\frac{2\kappa^3}{F}\right)^{2Z_c/\kappa - |m| - 1} e^{-2\kappa^3/3F}, \end{aligned} \tag{4.30}$$

where κ is related to the ionization energy I_p by $\kappa = \sqrt{2I_p}$, m is the projection of the electronic orbital angular momentum along the internuclear axis, F is the field strength. In Eq. 4.30, the parameters C_{lm} are determined from the valence electron wavefunction of the molecule in the asymptotic region and has been tabulated by Tong *et al.* [10]. To obtain the ionization rate by a laser, we need to average over the field strength of one-half cycle,

$$\begin{aligned} w(F) &= \frac{1}{\pi}\int_0^{\pi} w_{stat}(F\cos\tau)d\tau \\ &= \left(\frac{3F}{\pi\kappa^3}\right)^{1/2} w_{stat}(F), \end{aligned} \tag{4.31}$$

where F now stands for the peak field strength within the half cycle. If the molecule is aligned at an angle θ with respect to the laser polarization direction, the ionization rate is given by

$$w(F,\theta) = \sum_{m'} w(F), \tag{4.32}$$

with

$$\begin{aligned} B(m') &= \sum_l C_{lm} D^l_{m',m}(0,\theta,0) \\ &\quad \times(-1)^{m'}\sqrt{\frac{(2l+1)(l+|m'|)!}{2(l-|m'|)!}}, \end{aligned} \tag{4.33}$$

where the D-function reflects the rotation of the electronic wavefunction from the direction of the molecular axis to the laser polarization direction. In the MO-ADK model, Eq. 4.29 reduces to the traditional ADK model for atoms if ℓ is taken to be the orbital angular momentum quantum number of the valence electron. For diatomic molecules, the summation over ℓ is a consequence of expanding the two-center electronic wavefunction of a valence orbital in terms of single-center atomic orbitals. We note that the valence electron for N_2 is a σ_g orbital such that $m = 0$, while for O_2 it is a π_g orbital such that $m = 1$. The molecular parameters needed for performing these calculations for N_2 and O_2 molecules have been listed in [104].

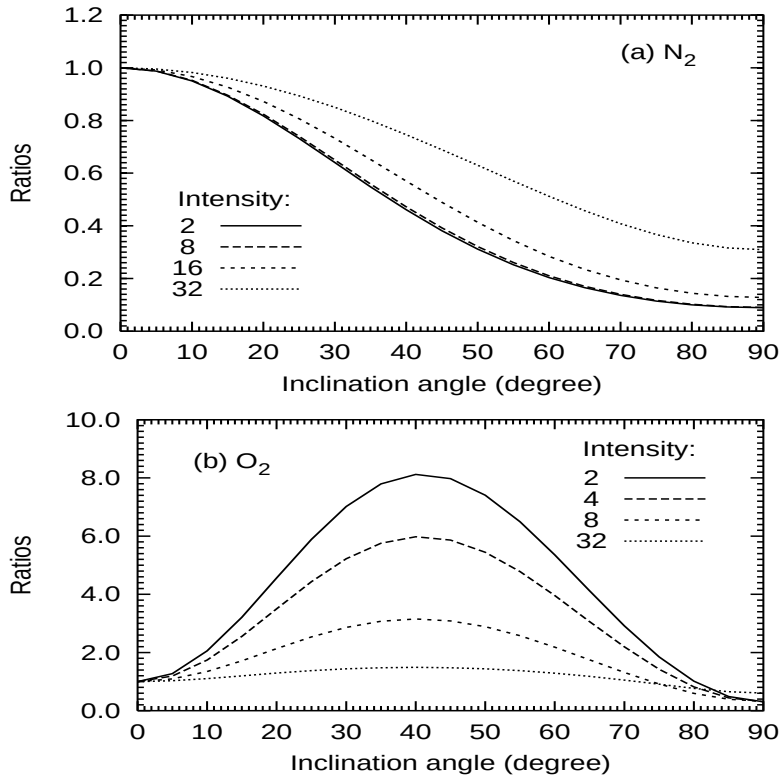

Figure 4.4. The ionization rates as a function of the angle θ between the laser field direction and the molecular axis for (a) N_2 and (b) O_2 molecules. The laser peak intensity is in units of 10^{13} W/cm^2. The rates are normalized at 0 degree.

In Fig. 4.4, we show the alignment-dependent ionization rates for N_2 and O_2 molecules at peak field intensities from 2×10^{13} W/cm^2 to 3.2×10^{14} W/cm^2, normalized with respect to θ=0. For N_2 the ionization rate decreases monotonically with increasing θ. This is not the case for O_2 molecules where the ionization rate peaks at θ near 40°. With higher field intensities the dependence of ionization rate versus θ becomes weaker.

These calculated alignment dependent ionization rates from the MO-ADK model can be qualitatively understood in terms of the geometry of the charge distribution of valence electrons for each molecule. For N_2, the valence electron is a σ_g orbital, and its electron cloud lies preferentially along the internuclear axis. Thus when the molecule is aligned

along the field direction, the electronic density along the field direction is maximum and the electron is most easily ionized. When the molecule is aligned at an angle θ with respect to the field, the effective electronic density in the field direction is reduced and the ionization rate becomes smaller. The situation for O_2 is different. Its valence electron is a π_g orbital. When the molecular axis coincides with the laser polarization direction, there is little valence electron density. On the other hand, when the field direction is at 45° with respect to the molecular axis, the electron cloud would have maximum density along the field direction and thus the ionization rate is maximum. The results in Fig. 4.4 are consistent with this simple geometric interpretation.

4.6 Alignment-dependent ionization

In the last decade, many experiments have been carried out with the aim of investigating the alignment dependence of the ionization rates of molecules using the Coulomb explosion technique [117, 118, 119, 120, 121, 122]. By detecting two dissociated ions in coincidence, the alignment of the molecule before ionization may be deducted. However, the Coulomb explosion technique works better if the molecular ions are doubly or multiply ionized by the laser. At present even single ionization of molecules is not well understood, not to mention multiple ionization[123]. Dissociative ionization may occur at different internuclear separations, and the ion products could also be deflected by the laser fields before they reach the detectors. These unknown factors make it difficult to extract quantitative alignment dependence of ionization rates from these experiments directly.

Here we consider a double-pulse experiment where the alignment dependent ionization rates for molecules predicted by the MO-ADK model [104] can be directly and unequivocally tested. A short pump pulse is used to generate a rotational wavepacket which produces aligned molecules during the periods of rotational wavepacket revival. The ionization probabilities by a subsequent probe laser vs the time-delay are calculated for O_2

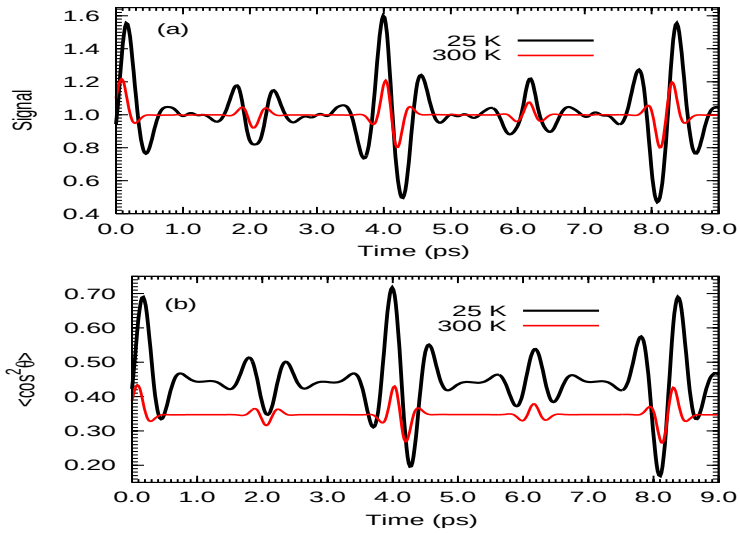

Figure 4.5. (a) Ionization signal as a function of the delayed time between the pump and probe laser pulses, and (b) time-dependent alignment parameters after the pump pulse for N_2 at 25 K and 300 K. The pump and probe laser intensities are 2×10^{13}W/cm^2 and 8×10^{13}W/cm^2, respectively.

and N_2 molecules at different temperatures. Distinct time dependence is presented and the results are interpreted in terms of the geometry of the charge distributions of the valence electrons of the two molecules.

The laser referred will always be the Ti:Sapphire laser set at 800 nm, assuming a Gaussian pulse shape. We take the pulse pulse intensity as 2×10^{13} w/cm^2 with optimal pulse duration 250 fs as discussed previously and probe pulse with intensity of 4×10^{13}W/cm^2 for O_2 and 8×10^{13}W/cm^2 for N_2.

In Fig. 4.5(b) the time-dependence of alignment of N_2 is shown at two temperatures. At 300 K, the molecules are not aligned except at several intervals during which the align-

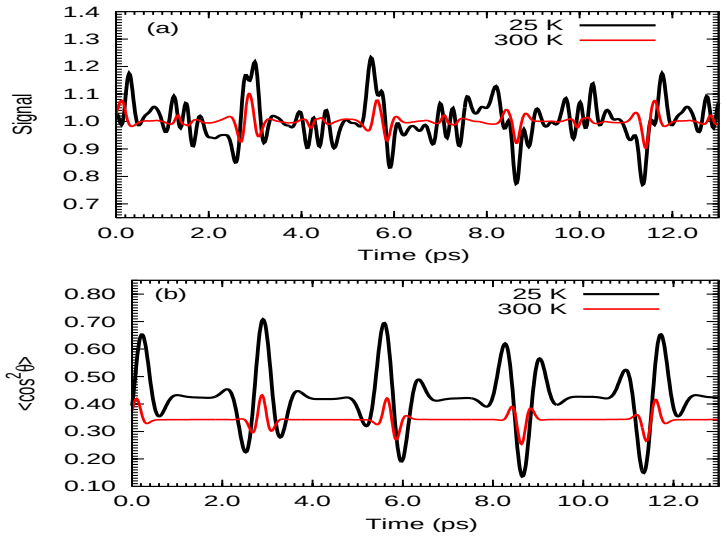

Figure 4.6. (a) Ionization signal as a function of the delayed time between the pump and probe laser pulses, and (b) time-dependent alignment parameters after the pump pulse for O_2 at 25 K and 300 K. The pump and probe laser intensities are 2×10^{13}W/cm^2 and 8×10^{13}W/cm^2, respectively.

ment changes rapidly. These rapid changes occur when the molecules experience rotational wavepacket revival, see the structures near 4 ps and 8 ps in Fig. 4.5(b). The rotational revival repeats at intervals separated by T_r, where T_r is determined by the rotational constant of the molecule. For N_2, the revival time is 8 ps. At each rotational revival, for a period of a few hundred femtoseconds, the alignment of molecules changes rapidly. The anisotropic distributions of molecules in this short time interval offer the opportunity to investigate the alignment dependence of ionization rates without the need of determining the alignment of each molecule. The degree of alignment for a given laser pulse increases if the molecules are at lower temperature.

By employing another "probe" laser at different time delays with respect to the weak "pump" laser, the ionization rates or signals from such aligned molecules can be measured. Consider a probe laser which has the same polarization direction as the pump laser. In Fig. 4.5(a) we show the predicted ionization signals at two temperatures when a second 25 fs "probe" pulse of peak intensity 8×10^{13} W/cm^2 is used to ionize the aligned molecules. Note that the ionization signals vary rapidly with the time delay. The ionization signal peaks when the alignment peaks. In fact, the time-dependence of the ionization signal almost mimics the time-dependence of the alignment of the molecules. This is no surprise since the alignment-dependent ionization rate for N_2, as shown in Fig. 4.4(a), is almost approximately given by $\cos^2\theta$. Since the degree of alignment is defined to be the average of $\cos^2\theta$, the two averages are essentially identical mathematical expressions. In terms of relative magnitudes, at 25 K, the maximum to the minimum peak signals is more than a factor of 3. At 300 K, the ratio still is about 1.42.

The ionization signal vs time delay for O_2 molecules is markedly different, especially at lower temperature, as shown in Fig. 4.6. Clearly the ionization signal does not peak at the time when the alignment is at the maximum. The reason is already given earlier. When O_2 molecules are aligned in the direction of the laser field, the density of the valence electron in the field direction is small. At each time delay, the molecules are distributed over a broad range of angles even if the molecules are aligned. At lower temperature the distribution becomes sharper, i.e., the molecules are distributed more sharply along the field direction. Thus, for example, at 25 K, the ionization signal is at a local minimum when the alignment is maximum. At higher temperature, the ionization signal does not change with time delay as strongly as in N_2. The ionization signal is the average of two functions. One is the distribution of the molecular alignment which peaks at θ=0°. The other is the alignment dependent ionization rate which peaks at θ near 45°. As a result, the ionization

signal does not depend on the alignment as strongly for O_2. At 25 K, the ratio of maximum to minimum ionization rates is 1.6, as compared to 3.0 for N_2.

So far we have chosen the polarization of the probe pulse to be parallel to the polarization of the "pump" pulse. An alternative method to test the prediction of the MO-ADK theory is to study the ionization signal vs the relative polarization direction. when the probe pulse is parallel to the pump pulse, the ionization signal is given by

$$P_{ion} = \int_0^{2\pi} \int_0^{\pi} |\psi(\theta, \phi)|^2 f(\theta) \sin\theta d\theta d\phi. \tag{4.34}$$

Since $\psi(\theta, \phi)$ has azimuthal symmetry, it can be reduced to

$$P_{ion} = 2\pi \int_0^{\pi} |\psi(\theta)|^2 f(\theta) \sin\theta d\theta, \tag{4.35}$$

where $f(\theta)$ is the ionization rate at the angle θ between polarization of laser pulse and molecular axis. When the the probe pulse is placed at θ_0 with respect to the pump pulse, the azimuthal symmetry is broken and the ionization signal in this situation is given by

$$P_{ion}(\theta_0) = \int_0^{2\pi} \int_0^{\pi} |\psi(\theta, \phi)|^2 f(\gamma) \sin\theta d\theta d\phi, \tag{4.36}$$

where γ is the angle between the molecular axis and the polarization of laser pulse, and

$$\cos\gamma = \sin\theta \cos\phi \sin(\theta_0) + \cos(\theta) \cos(\theta_0). \tag{4.37}$$

If we define

$$F(\theta) \quad = \quad \int_0^{2\pi} f(\gamma) d\phi, \tag{4.38}$$

the ionization signal can be written as

$$P_{ion}(\theta_0) = \int_0^{\pi} |\psi(\theta, \phi)|^2 F(\theta) \sin\theta d\theta. \tag{4.39}$$

In Fig. 4.7, we show the calculated dependence of the ionization signals at three different relative polarizations between the two laser pulses for O_2 at 25 K. At this low

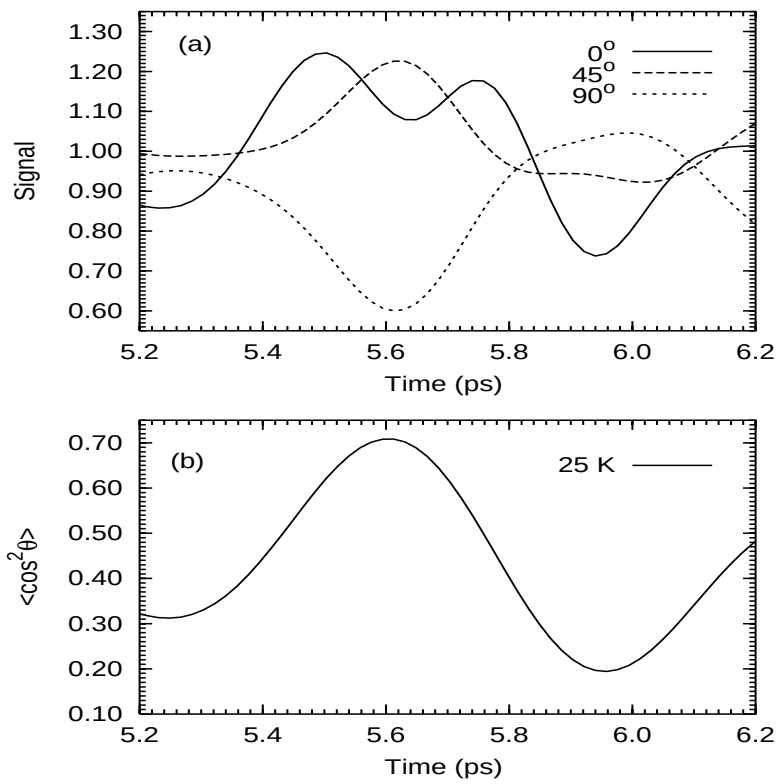

Figure 4.7. (a) Ionization signal as a function of the delayed time between the pump and probe laser pulses with different probe laser polarizations, and (b) time-dependent alignment parameter after the pump pulse for O_2 at 25 K. The pump and probe laser intensities are 2×10^{13}W/cm^2 and 8×10^{13}W/cm^2, respectively.

temperature and at the time of maximum alignment, the ionization signal is near maximum when the two polarizations are 45° with respect to each other. At the maximum alignment, the molecules are preferentially aligned in the direction of polarization of the "pump" laser. When the probe laser is set at 45° with respect to the pump laser, it is the direction where the charge density of the O_2 valence electron is maximum, and thus the ionization rate will be maximum. In this way, the directional property of the valence electron can be probed directly in a two-pulse experiment and such a method probably can be extended to study more complex molecules.

In summary we propose a double short-pulse laser experiment to measure the alignment dependent ionization probability of N_2 and O_2 molecules. A short weak pump pulse is used to align the molecules during the period where the molecules undergo rotational wavepacket revival. During this revival period a second "probe" pulse is used to ionize the molecules at different time delays. It is predicted that the ionization signal depends sensitively on the time delay. For N_2 maximum ionization was predicted to occur when the molecules have maximum alignment. For O_2, because its valence electron is a π orbital, the ionization signal is smaller when the alignment is at the maximum. The behavior predicted for O_2 should be applicable to other molecules with π valence electrons. Similarly, the predictions for N_2 should be characteristic of molecules with σ valence electrons. As noted previously [104] molecules whose valence electron is a π orbital would exhibit "ionization suppression". From the existing ionization measurements on diatomic molecules, the only molecule which has π valence electron but its ionization does not exhibit ionization suppression is the F_2 molecule. Following the distinctly predicted difference in O_2 and N_2, it may be desirable to perform double-pulse experiment on F_2 to check if the ionization rate of F_2 vs time delay is closer to that for O_2 or to N_2. The proposed double-pulse experiment would shed new light to test our understanding of the interaction of lasers with molecules.

Chapter 5

Summary and conclusions

In this dissertation, I have explored the dynamics of atoms and molecules in ultrashort laser fields. With pulse durations approaching attosecond time scale, attosecond metrology in capturing electronic processes occurring in matter-light interactions is becoming a reality. We have performed calculations of angle-resolved photoelectron spectra of Ar atoms in the combined field of an attosecond XUV pulse and a circularly polarized laser pulse. Electrons generated by the attosecond XUV pulse are deflected by the laser field. We examined first theoretically how the electron spectra, including the angular distributions, depend on the pulse duration and the chirp parameter of the XUV light pulse. We also showed how to retrieve or measure the pulse duration and the chirp parameter of such an attosecond XUV pulse if the angle-resolved electron spectra are available from experiments. The method requires that the few-cycle lasers be well characterized already, including the carrier envelope phase.

Applying the strong field approximation, we have developed a quantum theory for describing the photoelectron spectra of an autoionizing state created by an attosecond XUV pulse in the streaked few-cycle IR laser field. From the time-resolved spectra, we demonstrated how to monitor the dynamics of the decay process in a laser field and illustrated the utility of the theory by extracting the lifetime of one isolated and two nearby resonances.

We proposed a double short-pulse laser experiment to measure the alignment dependent ionization probability of N_2 and O_2 molecules. With a short pump pulse, the molecules undergo dynamic alignment at revival times. During this revival period, a second "probe" pulse is used to ionize the molecules at different time delays. We showed that the ionization signal is sensitive to the time delay. For N_2, maximum ionization was predicted to occur when the molecules have maximum alignment. For O_2, because its valence electron is a π

orbital, the ionization signal is smaller when the alignment is at its maximum. The behavior predicted for O_2 should be applicable to other molecules with π valence electrons. Similarly, the predictions for N_2 should be characteristic of molecules with σ valence electrons. Experiments of similar types have now been carried out.

With the rapid progress of the laser technology, the field of ultra-short laser pulses and/or ultra-intense laser fields is expected to continue to grow and find many applications in the coming years. It is an exciting frontier in sciences where new developments and new challenges are emerging every single day.

APPENDIX A

Conversion of units and definiton of parameters

• **Electric field:** 1 a.u.=5.142×10^9 V/cm.

• **Laser intensity:** 1 a.u.=3.51×10^{16} W/cm^2.

• **Time:** 1 a.u.=2.4189×10^{-17} s, 1 fs=41.341 a.u.

• **Frequency and Wavelength:** Frequency of 1 a.u. corresponds to wavelength of 45.565 nm. For a typical Ti:Sapphire laser with a wavelength of 800 nm, the corresponding frequency is 0.057 a.u. (1.55 eV) and the cycle period is 110 a.u. =2.7 fs.

• **Ponderomotive energy:** defined as the cycle averaged kinetic energy of a free electron in a monochromatic laser field, i.e.,

$$U_P = \frac{e^2 E_0^2}{4\omega^2},$$

where E_0 and ω are the field strength and frequency respectively. Note it is proportional to the field intensity and inversely proportional to the square of the laser frequency. For typical Ti:Sapphire lasers with wavelength 800 nm, the ponderomotive energy is 6 eV for the laser intensity of 1×10^{14} W/cm^2.

• **Keldysh parameter [5]:** defined as

$$\gamma = \sqrt{\frac{I_p}{2U_P}},$$

where I_p is the ionization potential and U_p is the ponderomotive energy. Ionization takes place through multiphoton ionization (MPI) when $\gamma > 1$, but tunneling ionization dominates if $\gamma < 1$.

APPENDIX B

Gauge transformation

In the length gauge, the time-dependent Shrödinger equation for an atom with a single active electron in the laser field is given by

$$i\frac{\partial\Psi(\vec{r},t)}{\partial t} = [-\frac{1}{2}\nabla^2 + V(\vec{r}) - q\vec{E}\cdot\vec{r}(t)]\Psi(\vec{r},t), \tag{B.1}$$

where q is the electronic charge. In the velocity gauge, it takes the form

$$i\frac{\partial\Psi(\vec{r},t)}{\partial t} = [-\frac{1}{2}\nabla^2 + V(\vec{r}) - \frac{q}{c}\vec{A}(t)\cdot\hat{p}]\Psi(\vec{r},t), \tag{B.2}$$

where $\vec{A}$ is the vector potential of the laser field and is given below. The wavefunction of a free electron moving in the laser field is described by the Volkov state which can be obtained analytically by the transformation from length gauge to acceleration gauge

$$\Psi_L = \exp\left(-i\frac{q}{c}\vec{A}\cdot\vec{r}\right)\exp\left(i\vec{p}\cdot\vec{\alpha} - i\mu\right)\Psi_A, \tag{B.3}$$

where

$$\begin{aligned}
\vec{A}(t) &= \vec{A}(0) - c\int_0^t \vec{E}dt', \\
\vec{\alpha}(t) &= \vec{\alpha}(0) + \frac{q}{c}\int_0^t \vec{A}dt', \\
\mu(t) &= \mu(0) + \frac{q^2}{2c^2}\int_0^t A^2 dt'.
\end{aligned} \tag{B.4}$$

This transformation can be easily understood classically. In the classical description, the motion of an electron is characterized by its position and velocity, $(\vec{r},\vec{v})$. When the laser field is applied, these change to $(\vec{r}-\vec{\alpha},\vec{v}+\frac{q}{c}\vec{A})$. By shifting the center of $(\vec{r},\vec{v})$ from (0,0) to $(\vec{\alpha},\frac{q}{c}\vec{A})$, the effect of the laser field is removed, and the electrons in this frame can be treated as freely propagating. This reference frame is called the Kramers-Henneberger (KH) frame, and the wavefunction is said to be in the acceleration gauge. In the KH frame, the TDSE becomes

$$i\frac{\partial\Psi_A(\vec{r},t)}{\partial t} = \left[-\frac{1}{2}\nabla^2 + V(\vec{r}-\vec{\alpha})\right]\Psi_A(\vec{r},t). \tag{B.5}$$

In the absence of the $V(\vec{r})$ potential, the solution of the TDSE is a plane wave. By transforming back to the length gauge, we obtain the usual Volkov state.

APPENDIX C

Program descriptions

C.1 Code package PSSO

Purpose: Calculating TDSE of an atom in external fields. This package is originally developed by Dr. XiaoMin Tong.

Methods: The pseudospectral method is used to discretize the Hamiltonian and the splitting-operator method is used for the propagation of the wavefunction.

Source files:

1. t03h.f: main program;
2. t03.h: head file specifying the parameters and dimension of arrays;
3. shap.f: input of the laser pulse shape and transformation from angular space to angular momentum space;
4. d01bcf.f: determination of Gaussian quadrature rules;
5. makefile: compiling file executed by make command;
6. t03.in: input data for t03h.f;

Compiling: By running "make" command, makefile is called and executable file e.x is generated if no compiling errors are reported. Common libraries mkl_lapack, mkl_p4 , pthread and Vaxlib are called which are all available on the intel machines. For further information, please check with Dr. Tong or go to B. D. Esry's homepage. An example of the makefile is given in the following:

```
LIB = -lmkl_lapack -lmkl_p4 -lpthread -Vaxlib
e.x : t03h.o shap.o d01bcf.o t03.h
        ifc -xW -tpp7 -132 t03h.o d01bcf.o shap.o -o e.x $(LIB)
t03h.o : t03h.f t03.h
        ifc -xW -tpp7 -132 -c t03h.f
shap.o : shap.f t03.h
        ifc -xW -tpp7 -132 -c shap.f
```

```
d01bcf.o :d01bcf.f
        ifc -c d01bcf.f
```

Explanations of the input data:

rmax:	maximum radial distance in a.u.
alpha:	dividing point of the inner and the outer region
rc:	smaller than rmax. An absorber is used beyond rc
nl:	number of partial waves used
nr:	number of grid points in radial dimension
tdl:	laser pulse duration in unit of fs
El0:	laser intensity in unit of 10^{14} w/cm^2
omegal:	laser frequency in unit of eV.

The rest data will only be used when another XUV pulse is accompanied with the laser field:

tdx:	XUV pulse duration in unit of fs
ex0:	XUV pulse intensity in unit of 10^{14} w/cm^2
omegax:	XUV photon energy in unit of eV
dealy:	time delay (in fs) between two pulses.

Sample of the input file: t03.in

```
400.d0     200.d0     390.d0     40     600     rmax, alpha, rc, nl, nr
10.0       4.0d-1     1.56       tdl (fs),El0(10^14),omegal(eV)
0.5        1.d-2      20         tdx (fs),ex0,omegax(ev)
0.d0       delay time in fs.
```

Output: The partial wavefunctions after the propagation are stored in the files fort.11 to fort.30 (10+nl). If the dipole moment is desired, the subroutine "resu" in t03h.f should be called, and the dipole moment will be stored in file t03.out. In order to calculate ATI

photoelectron spectra, addition file Couladqf.f can be used. The pre-calculated partial wavefunctions will served as the input data. The atomic potential in Couladqf.f should be consistent with that used in t03h.f.

C.2 Package ALIGN

Purpose: Calculating the alignment of molecules by a laser field.

Method: The splitting-operator method is used to solve the the timed-dependent Schrödinger equation of a molecule rotating in a laser field. Magnetic quantum number is conserved, thus the wavefuction can be expanded by spherical harmonic functions with given m number.

Source files: QMensemble.f, shap.f, t03.h, align.in, d01bcf.f, makefile and thermalaver.f.

Explanation of the input data:

nl:	number of partial waves;
theinertia:	the inertia of the molecule;
pola1, pola2:	principal component of the polarizability along and perpendicular to the molecular axis
frm:	laser field strength in a.u.
eof:	laser frequency in a.u.;
dt:	time step of propagation in a.u.
ncycle:	laser pulse duration in unit of the laser optical period.

Sample of the input file, align.in:

```
40          nl
0.023905        0.0577        50.1        90        frm, eof, dt,ncycle
54000.d0        theinertia
17.618        8.808        pola1,pola2
```

Output: The time-dependent alignment parameter for the initial $|JM>$ with $M \geq 0$ rotational state is stored in fort.(1000+indexJM) where indexJM is the sorting index of $|JM>$ state. If the density of the rotational wavepacket at time mt is wanted, the output files fort.(3000+mt) should be disclosed. For a given temperature, the thermal averaging is carried out using program thermalaver.f. The averaged alignment parameter is stored in align.dat.

C.3 Package LAAS

Purpose: Calculating laser-assisted autoionization spectra in a XUV pulse.

Method I: Under the strong field approximation, semi-analytical method to calculate laser-assisted autoionization spectra is implemented in FanoMay1.f with input file fano.in. The integration of the field is carried out first. For the second fold of integration, the interpolation method is used to find the time-varying vector potential and other quantities related to the field.

Sample of the input file, fano.in:

```
5.0    1.d-2    1.65        tdl(fs), El0(10^14), omegal(eV)
0.5    1.d-2    39.0         tdx(fs), ex0, omegax(ev)
0.d0        delay time in fs
0.d0        ellipticity
0.d0        phase in mutiples of π
1          2          controlling parameters: no. of resonances and iflag
16.121915          ionization potential in ev
      q,          position (eV)        width (eV)
-4.19199804    22.922855          0.055264
```

Method II. Numerical solving the time-dependent Schrödinger equation for a two-channel system is performed by generalizing the package PSSO. The source files include: t03h2c.f, shap.f, d01bcf.f, makefile and t03.in. The input data is the same as that used in PSSO. The two-channel continuum wavefunctions are calculated in adqf.f with input file adqf.in.

Explanation of variables and subroutines:

cphir(i,j), dphir(i,j):	wavefunctions in the lower and upper channel respectively, i, j represent the ith grid point and the jth partial wave
cphip, dphip:	wavefunctions of the lower and upper channel in the energy space respectively
sym_kin():	initialize the symmetrized kinetic operator
PRETRAN():	prepare the transform matrix between θ and L space
tran_pre(), :	prepare the transform matrix between coordinate space and energy space for lower channel
tran_pre_II():	prepare the transform matrix between coordinate space and energy space for upper channel
WF_pre(ier):	prepare the initial wavefunction
proinv1():	transformation between coordinate space and energy space
proinV2():	transformation between θ and L space
time_pro():	coupling between two channels.

C.4 Package LAPI

Purpose: Calculating the laser-assisted photoionization spectra.

Method: The laser-assisted photoelectron spectra is calculated using LAPI_numXecton.f. The input file is Omega.in and Xection.dat. The photoionization cross section and the

asymmetry parameter is precalculated and stored in Xection.dat. In order to obtain the information of the XUV pulse from the spectra, the genetic algorithm is implemented in the code InvLAPI3.f and ga170.f.

Compiling: run "make" command to call the makefile. Content of the makefile:

```
InvLAPI.x : InvLAPI3.f LAPI.h LAPI.x ga170.o
        ifc InvLAPI3.f ga170.o -o InvLAPI.x
LAPI.x : LAPI_num_cir.f LAPI.h
        ifc LAPI_num_cir.f -o LAPI.x
ga170.o: ga170.f params.f LAPI.h
        ifc -c ga170.f
```

Sample of the input file, Omga.in:

5.d0	1.d-1	1.653	tdl(fs), El0(10^{14}), omegal(eV)
0.05	1.d-2	35	tdx(fs),ex0,omegax(ev)
0.d0	delay time in fs		
1.d0	ellipticity		
15.759	ionization potential (eV).		

REFERENCES

[1] K. Burnett, V. C. Reed, and P. L. Knight, J. Phys. B **26**, 561 (1993).

[2] M. Protopapas, C. H. Keitel, and P. L. Knight, Rep. Prog. Phys. **60**, 389 (1997).

[3] T. Brabec and F. Krausz, Rev. Mod. Phys. **72**, 545 (2000).

[4] P. Agostini and L. F. DiMauro, Rep. Prog. Phys. **67**, 813 (2004).

[5] L. V. Keldysh, Sov. Phys. JETP **20**, 1307 (1965).

[6] M. V. Ammosov, N. B. Delone, and V. P. Krainov, Sov. Phys. JETP **64**, 1191 (1986).

[7] P. B. Corkum, Phys. Rev. Lett. **71**, 1994 (1993).

[8] A. Becker and F. H. M. Faisal, Phys. Rev. Lett. **84**, 3546 (2000).

[9] B. Feuerstein, R. Moshammer, and J. Ullrich, J. Phys. B **33**, L823 (2000).

[10] X. M. Tong, Z. X. Zhao, and C. D. Lin, Phys. Rev. A **66**, 033402 (2002).

[11] P. Agostini, F. Fabre, G. Mainfray, and N. K. Rahman, Phys. Rev. Lett. **42**, 1127 (1979).

[12] E. Cormier *et al.*, J. Phys. B **34**, L9 (2001).

[13] B. Borca, M. Frolov, N. L. Manakov, and A. F. Starace, Phys. Rev. Lett. **87**, 133001 (2001).

[14] G. G. Paulus, F. Grasbon, H. Walther, R. Kopold, and W. Becker, Phys. Rev. A **64**, 021401 (2001).

[15] K. C. Kulander, K. J. Schafer, and J. L. Krause, in *Super Intense Laser Atom Physics*, edited by B. Piraux, A. L'Huillier, and K. Rzazewski, Series B Vol. 316, p. 95, New York, 1993.

[16] K. J. Schafer, B. Yang, L. F. DiMauro, and K. C. Kulander, Phys. Rev. Lett. **70**, 1599 (1993).

[17] J. K. Krause, K. J. Schafer, and K. C. Kulander, Phys. Rev. A **45**, 4998 (1992).

[18] M. Lewenstein, P. Balcou, M. Y. I. ad Anne L'Huillier, and P. B. Corkum, Phys. Rev. A **49**, 2117 (1994).

[19] Z. Chang, A. Rundquist, H. Wang, M. M. Murnane, and H. C. Kapteyn, Phys. Rev. Lett. **79**, 2967 (1997).

[20] E. A. Gibson *et al.*, Phys. Rev. Lett. **92**, 033001 (2004).

[21] P. Antonie, A. L'Huillier, and M. Lewenstein, Phys. Rev. Lett. **77**, 1234 (1996).

[22] P. M. Paul *et al.*, Science **292**, 1689 (2001).

[23] L. C. Dinu *et al.*, Phys. Rev. Lett. **91**, 063901 (2003).

[24] I. P. Christov, M. M. Murnane, and H. C. K. Kapteyn, Phys. Rev. Lett. **78**, 1251 (1997).

[25] K. J. Schafer and K. C. Kulander, Phys. Rev. Lett. **78**, 638 (1997).

[26] C. Kan, N. B. Burnett, C. E. Capjack, and R. Rankin, Phys. Rev. Lett. **79**, 2971 (1997).

[27] M. Ivanov, P. B. Corkum, T. Zuo, and A. Bandrauk, Phys. Rev. Lett. **74**, 2933 (1995).

[28] V. T. Platonenko and V. V. Strelkov, J. Opt. Soc. Am. B **16**, 435 (1999).

[29] Z. Chang, Phys. Rev. A **70**, 043802 (2004).

[30] G.Tempea, M. Geissler, and T. Brabec, J. Opt. Soc. Am. B **16** (1999).

[31] Z. Zeng, R. Li, W. Yu, and Z. Xu, Phys. Rev. A **67**, 013815 (2003).

[32] E. Cormier and P. Lambropoulos, Eur. Phys. J. D **2**, 15 (1998).

[33] I. P. Christov, Opt. Lett. **24**, 1425 (1999).

[34] S. Chelkowski and A. Bandrauk, Phys. Rev. A **65**, 061802 (2002).

[35] A. Apolonski *et al.*, Phys. Rev. Lett. **85**, 740 (2000).

[36] D. J. Jones *et al.*, Science **288**, 635 (2000).

[37] A. Baltuška *et al.*, Nature (London) **421**, 611 (2003).

[38] P. Dietrich, F. Krausz, and P. B. Corkum, Opt. Lett. **25**, 16 (2000).

[39] G. Steinmyer, Science **286**, 1507 (1999).

[40] M. Drescher *et al.*, Nature (London) **419**, 803 (2002).

[41] J. M. Schins *et al.*, Phys, Rev. Lett. **73**, 2180 (1994).

[42] T. E. Glover, R. W. Schoenlein, A. H. Chin, and C. V. Shank, Phys. Rev. Lett. **76**, 2468 (1996).

[43] M. Kitzler, N. Milosevic, A. Scrinzi, F. Krausz, and T. Brabec, Phys. Rev. Lett. **88**, 173904 (2002).

[44] J. Itatani *et al.*, Phys. Rev. Lett. **88**, 173903 (2002).

[45] M. Hentschel *et al.*, Nature (London) **414**, 509 (2001).

[46] M. Drescher *et al.*, Science **291**, 1923 (2001).

[47] R. Kienberger *et al.*, Science **297**, 1144 (2002).

[48] E. Goulielmakis *et al.*, Science **305**, 1267 (2004).

[49] S. A. Aseyev, Y. Ni, L. J. Frasinski, H. G. Muller, and M. J. J. Vrakking, Phys. Rev. Lett. **91**, 223902 (2003).

[50] O. Smirnoiva, V. S. Yakovlev, and A. Scrinzi, Phys. Rev. Lett. **91**, 253001 (2003).

[51] M. Wickenhauser and J. Burgdörfer, Laser Phys. **14**, 492 (2004).

[52] Z. X. Zhao and C. D. Lin, Phys. Rev. A (2005).

[53] J. H. Posthumus, Rep. Prog. Phys. **67**, 623 (2004).

[54] H. Stapelfeldt and T. Seideman, Rev. Mod. Phys. **75**, 543 (2003).

[55] A. Talebpour, C. Y. Chien, and S. L. Chin, J. Phys. B **29**, L667 (1996).

[56] A. Talebpour, S. Larochelle, , and S. L. Chin, J. Phys. B **31**, L49 (1998).

[57] C. Guo, Phys. Rev. Lett. **85**, 2276 (2000).

[58] M. J. DeWitt, E. Wells, and R. R. Jones, Phys. Rev. Lett. **87**, 153001 (2001).

[59] E. Wells, M. J. DeWitt, and R. R. Jones, Phys. Rev. A **66**, 013409 (2002).

[60] B. Shan, X.-M. Tong, Z. Zhao, Z. Chang, and C. D. Lin, J. Phys. B **66**, 061401 (2002).

[61] Z. X. Zhao, X. M. Tong, and C. D. Lin, Phys. Rev. A **67**, 043404 (2003).

[62] I. Litvinyuk *et al.*, Phys. Rev. Lett. **90**, 233003 (2003).

[63] P. W. Dooley *et al.*, Phys. Rev. A **68**, 023406 (2003).

[64] X. M. Tong *et al.*, J. Phys. B **38**, 333 (2005).

[65] A. S. Alnaser *et al.*, Phys. Rev. A **71**, 031403(R) (2005).

[66] P. H. Bucksbaum, A. Zavriyev, H. G. Muller, and D. W. Schumacher, Phys. Rev. Lett. **64**, 1883 (1990).

[67] A. D. Bandrauk and M. L. Sink, J. Chem. Phys. **74**, 110 (1981).

[68] T. Zuo and A. D. Bandrauk, Phys. Rev. A **52**, R2511 (1995).

[69] H. Niikura *et al.*, Nature (London) **417**, 917 (2002).

[70] X. M. Tong, Z. X. Zhao, and C. D. Lin, Phys. Rev. Lett. **91**, 233203 (2003).

[71] A. S. Alnaser *et al.*, Phys. Rev. Lett. **91**, 16302 (2003).

[72] J. Itatani *et al.*, Nature **432**, 867 (2004).

[73] P. B. Corkum, N. H. Burnett, and M. Y. Ivanov, Opt. Lett. **19**, 1870 (1994).

[74] P. Antonie, B. Piraux, D. B. Milosevic, and M. Gajda, Phys. Rev. A **54**, R1761 (1996).

[75] V. Strekov *et al.*, Appl. Phys. B **78**, 879 (2004).

[76] B. Shan, S. Ghimire, and Z. Chang, J. Modern. Optics **52**, 277 (2004).

[77] F. H. Faisal, J. Phys. B **6**, L689 (1973).

[78] H. R. Reiss, Phys. Rev. A **22**, 1786 (1980).

[79] M. Nurhuda, F. H. M. Faisal, and U. Schwengelbeck, Computer Physics Communications **134**, 291 (2001).

[80] A. Becker and F. H. Faisal, Phys. Rev. A **59**, R1742 (1999).

[81] J. Muth-Böhm, A. Becker, and F. H. M. Faisal, Phys. Rev. Lett. **85**, 2280 (2000).

[82] E. S. Toma and H. G. Muller, J. Phys. B **35**, 3435 (2002).

[83] D. J. Kennedy and S. T. Manson, Phys. Rev. A **5**, 227 (1972).

[84] F. A. Parpia, W. R. Johnson, and V. Radojevic, Phys. Rev. A **29**, 3173 (1984).

[85] M. Y. Adam, P. Morin, and G. Wendin, Phys. Rev. A **31**, 1426 (1985).

[86] R. Trebino *et al.*, Rev. Sci. Instrum. **68**, 3277 (1997).

[87] A. H. Zewail, J. Phys. Chem. **104**, 5660 (2000).

[88] M. Wickenhauser, J. Burgdörfer, F. Krausz, and M. Drescher, Phys. Rev. Lett. **94**, 023002 (2005).

[89] A. Starace, Phys. Rev. A **16**, 231 (1977).

[90] U. Fano, Phys. Rev. **124**, 1866 (1961).

[91] M. Aymar, C. H. Greene, and E. Luc-Koenig, Rev. Mod. Phys. **68**, 1015 (1996).

[92] L. Ixaru, Comp. Phys. Comm **147**, 834 (2002).

[93] T. Morishita *et al.*, J. Phys. B **34**, L475 (2001).

[94] X. M. Tong and S. I. Chu, Chem. Phys. **217**, 1191 (1997).

[95] X.-M. Tong and S.-I. Chu, Phys. Rev. A **61**, 031401 (2000).

[96] X. M. Tong and C. D. Lin, Phys. Rev. Lett. **92**, 223003 (2004).

[97] H. Stapelfeldt, H. Sakai, E. Constant, , and P. B. Corkum, Phys. Rev. Lett. **79**, 2787 (1997).

[98] S. Chelkowski, P. B. Corkum, and A. D. Bandrauk, Phys. Rev. Lett. **82**, 3416 (1999).

[99] J. J. Larsen, K. Hald, N. Bjerre, and H. Stapelfeldt, Phys, Rev. Lett. **85**, 2470 (2000).

[100] S. M. Hankin, D. M. Villeneuve, P. B. Corkum, and D. M. Rayner, Phys. Rev. Lett. **84**, 5082 (2000).

[101] R. Velotta, N. Hay, M. B. Mason, M. Castillejo, and J. P. Marangos, Phys. Rev. lett. **87**, 183901 (2001).

[102] M. Plummer and J. F. McCann, J. Phys. B **30**, L401 (1997).

[103] S. C. Althorpe and T. Seideman, J. Chem. Phys. **110**, 147 (1999).

[104] X. M. Tong, Z. X. Zhao, and C. D. Lin, J. Phys. B **36**, 1121 (2002).

[105] A. D. Bandrauk and J. Ruel, Phys. Rev. A **59**, 2153 (1999).

[106] T. Seideman, Phys. Rev. Lett. **83**, 4901 (1999).

[107] J. Ortigoso, M. Rodríguez, M. Gupta, and B. Friedrich, J. Chem. Phys. **110**, 3870 (1999).

[108] L. Cai, J. Marango, and B. Friedrich, Phys. Rev. Lett. **86**, 775 (2001).

[109] C. M. Dion *et al.*, Phys. Rev. A **65**, 063408 (2002).

[110] P. Hering and C. Cornaggia, Phys. Rev. A **59**, 2836 (1999).

[111] S. Banerjee, G. R. Kumar, and D. Mathur, Phys. Rev. A **60**, R3369 (1999).

[112] B. Friedrich and D. Herschbach, Phys. Rev. Lett. **74**, 4623 (1995).

[113] B. Friedrich and D. Herschbach, J. Phys. Chem. **99**, 15686 (1995).

[114] K. F. Lee, D. M. Villeneuve, P. B. Corkum, and E. A. Shapiro, Phys. Rev. Lett. **93**, 233601 (2004).

[115] R. A. Bartels *et al.*, Phys. Rev. Lett. **88**, 013903 (2002).

[116] B. M. Smirnov and M. I. Chibisov, Sov. Phys. JETP **22**, 585 (1966).

[117] Z. Vager, R. Naaman, and E. P. Kanter, Science **244**, 426 (1989).

[118] P. Dietrich, D. T. Strickland, M. Laberge, and P. B. Corkum, Phys. Rev. A **47**, 2305 (1993).

[119] D. Normand, L. A. Lompré, and C. Cornaggia, J. Phys. B **25**, L497 (1992).

[120] J. H. Posthumus *et al.*, J. Phys. B **31**, L985 (1998).

[121] J. H. Posthumus *et al.*, J. Phys. B **31**, L553 (1998).

[122] L. Quaglia, M. Brewczyk, and C. Cornaggia, Phys. Rev. A **65**, 031404 (2002).

[123] S. V. Menon, J. P. Nibarger, and G. N. Gibson, J. Phys. B **35**, 2961 (2002).